POST-PROCESSING OF INSAR PERSISTENT SCATTERER TIME-SERIES TO INVESTIGATE DEFORMATIONAL PROCESSES INDUCED BY SUBSURFACE EXCAVATION

FINAL PROJECT REPORT

UCT-UTI Report 011

by
Wnuk K[1]
Zhou W[1]
Gutierrez M[1]
[1]Colorado School of Mines

Sponsorship
UTC-UTI

For

University Transportation Center for
Underground Transportation Infrastructure
(UTC-UTI)

September 30, 2021

Disclaimer

1. Report No.	2. Government Accession No.	3. Recipient's Catalog No.	
4. Title and Subtitle POST-PROCESSING OF INSAR PERSISTENT SCATTERER TIME-SERIES TO INVESTIGATE DEFORMATIONAL PROCESSES INDUCED BY SUBSURFACE EXCAVATION		5. Report Date September 2021 6. Performing Organization Code	
7. Author(s) Kendall Wnuk (Orcid.org/0000-0001-7499-5256) Marte Gutierrez (Orcid.org/0000-0001-5070-8726) Wendy Zhou (Orcid.org/0000-0001-8226-375X)		8. Performing Organization Report No. UTC-UTI Report 011	
9. Performing Organization Name and Address University Transportation Center for Underground Transportation Infrastructure (UTC-UTI) Tier 1 University Transportation Center Colorado School of Mines Coolbaugh 308, 1012 14th St., Golden, CO 80401		10. Work Unit No. (TRAIS) 11. Contract or Grant No. 69A355174711	
12. Sponsoring Agency Name and Address United States of America Department of Transportation Research and Innovative Technology Administration		13. Type of Report and Period Covered 14. Sponsoring Agency Code	
15. Supplementary Notes Report also available at: https://www.mines.edu/uct-uti and https://zenodo.org/communities/utc-uti			
16. Abstract Over the past 30 years, space-based geodetic measurements have become mainstream by applying Interferometric Synthetic Aperture Radar (InSAR). Standard InSAR time-series analyses can extract phase-based measurements of surface deformation with sub-centimeter, in some cases even sub-millimeter, accuracy. However, the standard analyses can only make measurements within a single viewing geometry, i.e., the Line Of Sight (LOS) of the sensor. Additionally, these analyses can be impacted by noise when applied to vegetated areas or tropical areas subject to turbulent atmospheric changes. The research projects described in this report are designed to take advantage of a new generation of temporally dense, multi-angle InSAR measurements by developing novel post-processing algorithms to reduce remaining data noise and resolve tunneling-induced subsidence in three dimensions. Findings from these projects are organized into the following three chapters: (1) Application of a novel 4-D filtering algorithm, designed to remove phase noise from InSAR data acquired in highly vegetated, tropical locations, to a widespread subsidence event in the highlands of Sri Lanka. (2) Adaptation of previously published algorithms that resolve satellite InSAR measurements into vertical and horizontal motion through a case study of subsidence events in Seattle, Washington, USA to reveal heterogeneous rebound and additionally delayed subsidence. (3) A novel modification to the minimum-acceleration algorithm allowing it to combine multiplatform SAR data, especially to ingest airborne InSAR data, and produce true 3D (Vertical, East-West, and North-South) deformation time series of a small magnitude, spatially acute tunneling-induced subsidence event in Los Angeles, California, USA. Algorithm results are shown to produce accurate and precise data, and results provide new insights into deformation processes induced by tunneling activities.			
17. Key Words Synthetic Aperture Radar; Tunneling; Groundwater; Subsidence; Remote Sensing; Excavation		18. Distribution Statement No restrictions.	
19. Security Classification (of this report) Unclassified	20. Security Classification (of this page) Unclassified	21. No of Pages 80	22. Price NA

TABLE OF CONTENTS

LIST OF FIGURES

LIST OF TABLES

EXECUTIVE SUMMARY

As subsurface excavation technologies continue to advance, tunneling has become increasingly common for both transportation and energy production applications. This necessitates the ability to monitor excavation-induced subsidence over large areas in a wide range of geologic and hydrologic settings, especially when ground-based measurements are unavailable. Over the past 30 years, space-based geodetic measurements have become mainstream by applying Interferometric Synthetic Aperture Radar (InSAR). Standard InSAR time-series analyses can extract phase-based measurements of surface deformation with sub-centimeter, in some cases even sub-millimeter, accuracy. However, the standard analyses can only make measurements within a single viewing geometry, i.e., the Line Of Sight (LOS) of the sensor. Additionally, these analyses can be impacted by noise when applied to vegetated areas or tropical areas subject to turbulent atmospheric changes. High-resolution InSAR data from a new generation of satellites offer the opportunity to post-process InSAR time-series data and reduce noise. The research projects described in this report are designed to take advantage of a new generation of temporally dense, multi-angle InSAR measurements by developing novel post-processing algorithms to reduce remaining data noise and resolve tunneling-induced subsidence in three dimensions. The report illustrates through three case studies how post-processing of large, temporally dense LOS InSAR time-series datasets can reduce interferometric noise to more accurately and precisely map and measure subsidence in both natural and urban environments. Findings from these projects are organized into the following three chapters: (1) Application of a novel 4-D filtering algorithm, designed to remove phase noise from InSAR data acquired in highly vegetated, tropical locations, to a widespread subsidence event in the highlands of Sri Lanka. (2) Adaptation of previously published algorithms that resolve satellite InSAR measurements into vertical and horizontal motion through a case study of subsidence events in Seattle, Washington, USA to reveal heterogeneous rebound and additionally delayed subsidence. (3) A novel modification to the minimum-acceleration algorithm allowing it to combine multiplatform SAR data, especially to ingest airborne InSAR data, and produce true 3D (Vertical, East-West, and North-South) deformation time series of a small magnitude, spatially acute tunneling-induced subsidence event in Los Angeles, California, USA. Algorithm results are shown to produce accurate and precise data, and results provide new insights into deformation processes induced by tunneling activities.

Post-processing through either 4-D filtering or application of the MinA algorithm revealed the true extent of surface displacements that were previously unrecognized or not captured by ground-based data. Knowing the full extent, duration, and magnitude of excavation-induced subsidence can be crucial to mitigating their potential impacts. This research highlights the need for space based geodetic monitoring of tunneling projects, and offers practical solutions for its application. As more SAR platforms become available, including the recent launch of the SAOCOM SAR constellation and future launch of NASA-ISRO SAR mission, post-processing algorithms can be used to combine data from multiple SAR inputs to compare to or potentially replace ground based geodetic systems for monitoring purposes.

CHAPTER 1 - INTRODUCTION

The increasing need for underground infrastructure in a wide range of environmental settings, especially tunneling for transportation systems in urban environments, has promoted the need for research projects like those included in this report. Tunnels are artificial underground passageways excavated through soil or rock that are prone to inducing surface subsidence through a combination of subsurface stress redistribution or disruption to the surrounding groundwater regime. Ground settlements of sufficient magnitude are capable of damaging overlying infrastructure, and it is therefore critical to control the ground subsidence within a certain limit. This places a heightened need on monitoring tunneling-induced ground settlement in a timely fashion in order to mitigate the potential adverse impacts.

Interferometric Synthetic Aperture Radar (InSAR) is a unique geodetic tool for measuring the deformation of the Earth's surface. In favorable environments, satellite InSAR can achieve millimeter-scale accuracy and precision, and has demonstrated the capability to measure excavation-induced subsidence in a wide range of geological settings [1–6]. SAR data first became available to the scientific community after the launch of the first European Remote Sensing (ERS-1) satellite in July 1991 (Figure 1.1) and was proven to be an effective geodetic tool after imaging deformation caused by the 1992 Landers earthquake [7]. By 2012, the Japanese (JERS, ALOS), Italian (COSMO-SkyMed), German (TerraSAR-X), and Canadian (RADARSAT-1 & 2) space agencies had launched their own SAR satellites, though data are mostly only available through commercial purchase. NASA's Uninhabited Aerial Vehicle SAR (UAVSAR) is an airborne sensor that began making acquisitions in 2009, but only makes repeat flights in limited locations a few times per year. With the launch of the European Space Agency's Sentinel-1A satellite in 2014, contemporary InSAR data is freely available for the first time, making it a viable option for monitoring surface displacements induced by tunneling activities and for studying long-term impacts. This coincides with an increase in tunneling projects around the world fueled by the need for underground infrastructure as well as the advancement of technologies like the Tunnel Boring Machine (TBM), which make underground excavations progress faster, safer, and cause less disturbance to surrounding soil or rock. The research projects included in this report aim to take advantage of this new generation of InSAR satellite data by developing novel post-processing methods designed to combine temporally dense datasets with time series processing techniques in order to more accurately quantify subsidence and/or rebound during the construction of underground infrastructure in both natural and urban environments.

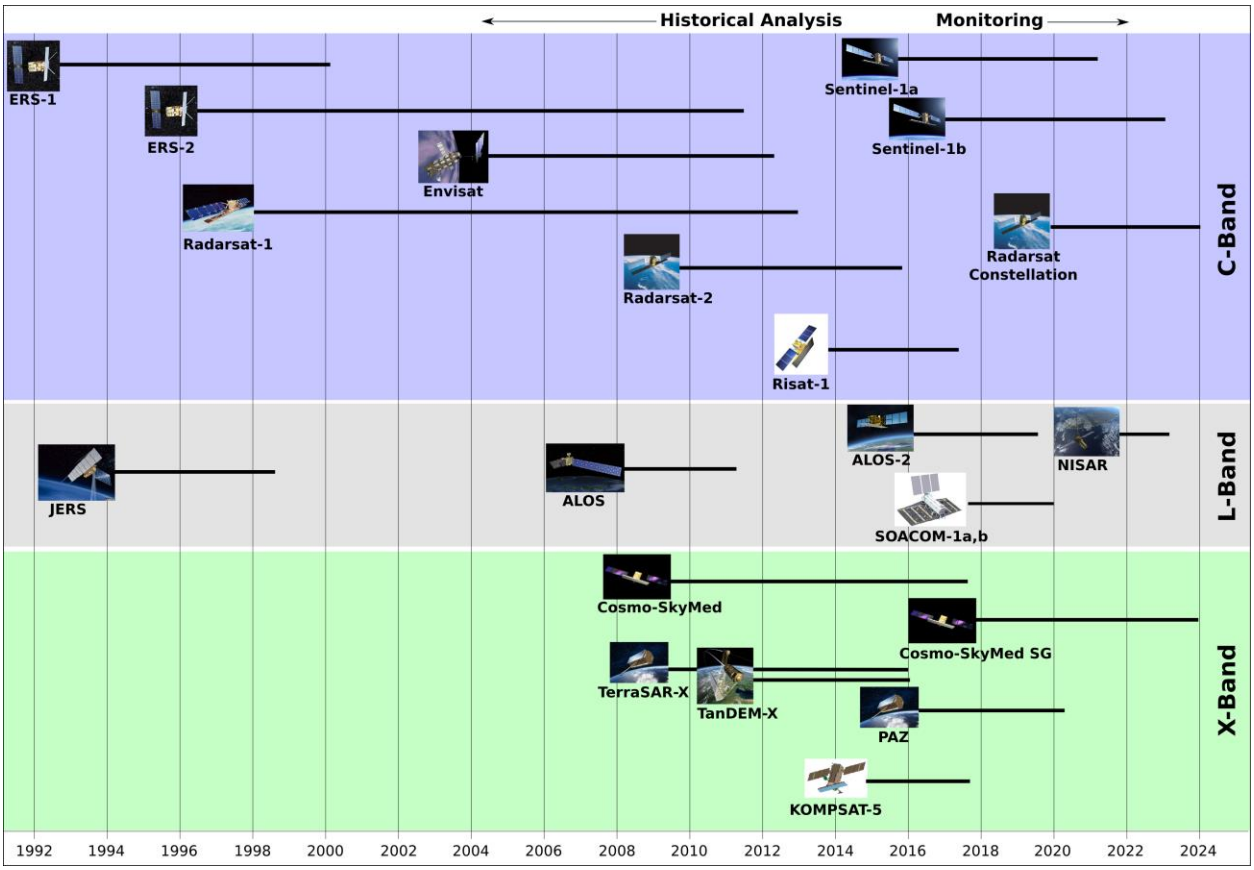

Figure 1.1 Timeline of past, present, and future SAR satellite launches. Image from UNAVCO

1.1 Motivation

Since the launch of Sentinel-1 satellites A and B in 2014 and 2016, respectively, weekly InSAR data are now freely available for any location. The majority of Sentinel-1 data is acquired in ScanSAR mode, an acquisition technique in which the sensor rotates to simultaneously scan multiple swaths and provide greater ground coverage. The combination of using multiple satellites in ScanSAR acquisition mode significantly enhances the temporal resolution of Sentinel-1, making it a useful data source to fill in time gaps of other SAR datasets. It uses C-band wavelength (~5.6 cm) sensor that provides data can be comparable to both X-band (~2 cm) sensors such as COSMO-SkyMed and L-band (~21 cm) sensors like UAVSAR. The launch of the Sentinel-1 constellation comes at a time when tunneling activities are globally increasing in frequency, and the environments in which they occur become more diverse. The proposed report focuses on novel ways to take advantage of this new generation of InSAR satellites that maintain a high temporal resolution over long periods of time. The abundance of data allows for the development of noise reduction filters, algorithms that calculate displacements in 3D, and provides the ability to examine deformation processes through the entirety of their duration.

1.2 Excavation Induced Surface Deformation

Surface deformations caused by tunneling can range greatly in magnitude and spatial extent, and are primarily influenced by the surrounding geology and hydrologic setting. Most often, the largest tunneling-induced surface settlements are observed above deep (>200m) tunnels excavated through fractured crystalline rock [2,3,8,9]. Settlement magnitudes can exceed 10cm [8] due to a consolidation mechanism whereby sustained or excessive water ingress at the excavation face leads to pore pressure drawdown and subsequent closure of fractures within the overlying rockmass [3,9]. Settlements encountered from tunneling in urban environments are generally lower in magnitude due to precautions made to reduce the risk of damaging overlying infrastructure. The surficial extent of deformation is dependent upon the size and depth of excavation, local geology, and presence of groundwater. In cases of excessive ingress or dewatering, the lateral extent of subsidence is controlled by groundwater storage geometry [6,9]; whereas, in dry conditions, the settlement is usually limited to areas directly overlying the excavation itself [1,4,5].

1.3 Standard and Novel InSAR Methods

Previous literature demonstrates the ability of InSAR to accurately measure surface deformation induced by underground excavation using a variety of processing techniques [1–6]. The most basic application of the SAR is the interferometry technique [10,11], which relies on measurements of the phase difference between two complex-valued SAR images acquired from similar orbital positions at different times. The measured phase difference (interferometric phase) can then be converted to physical units of displacement using a sensor of known wavelength. This simple 2-pass interferometry technique can be useful for identifying large magnitude, temporally discreet deformation events, but are subject to noise sources introduced by orbital deviations, topography, changes in atmospheric water vapor content, and random error. Advanced multi-pass InSAR techniques were developed to track the temporal evolution of deformation by combining sequences of differential SAR interferograms to quantify and remove some sources of phase noise. There are two types of advanced InSAR techniques for deformation time-series generation, including Persistent Scatterer (PS) [12,13] and Small Baseline (SBAS) techniques [14]. These InSAR time-series processing techniques have become standard practice over the past 20 years. Still, they are subject to phase noise from turbulent atmospheric effects, and cannot by themselves overcome the fact that a single SAR dataset can measure displacements only in a single Line Of Sight (LOS) projection.

As data from more sensors at greater spatial and temporal resolutions become available, the question arises, how are complementary pieces of information within separate SAR datasets most effectively combined? The combination of data from multiple SAR platforms, and therefore from different LOS vectors, can improve our ability to resolve the 3-D, i.e., East, North, and Up, components of the observed surface displacements. One method designed to combine overlapping segments of SAR images to generate high spatiotemporal resolution maps of the (combined) LOS displacement

field is known as the Multiple-SBAS (MSBAS) algorithm. This algorithm consists of generating and simultaneously processing a considerable sequence of multiple-platform differential SAR interferograms [15], and can produce a time series of the Up-Down (U-D) and East-West (E-W) displacement, but assumes the North-South (N-S) deformation is negligible due to lack of LOS sensitivity from satellites travelling along polar orbits.

More recently, the development of the Minimum-Acceleration (MinA) algorithm has allowed for 3D displacement calculation as a post-processing step using multiple InSAR time-series datasets as input [16–18]. The preliminary LOS InSAR time-series displacements are connected to unknown 3-D velocities among consecutive time acquisitions. This leads to the writing of an underdetermined system of independent linear equations, which is regularized by imposing the constraint that the 3-D displacement components are with minimum acceleration. Once estimated, the 3-D velocities are independently time integrated to recover the N-S, E-W and U-D deformation time series. Similar methods are being applied mostly in areas characterized by the presence of significant deformation signals (e.g., volcanic or co-seismic deformation), but have not been extensively tested on events with low-to-moderate magnitude deformations (e.g., tunneling-induced ground subsidence) [18].

1.4 Report Organization

This report is composed of five chapters. Chapter 1 (this chapter) states the research problem, addresses the background and significance of the research topic, and includes a discussion of previous work on the subject. The following four chapters present a body of work contributing an improvement to post-processing methods of InSAR time-series for application to subsidence induced by tunneling activities. Chapters 2, 3, and 4 present three independent manuscripts that have been submitted to or published within peer-reviewed scientific journals.

Chapter 2 presents a 4D filtering method for post-processing InSAR Persistent Scatterers. When using InSAR in tropical locations in particular, tropospheric noise caused by variations in pressure, temperature, and relative humidity are capable of obscuring signals of interest [19,20]. Because atmospheric noise does not correlate in time, it is often highly difficult to separate that phase contribution from the desired deformation signal. The novel 4D filtering method takes advantage of the high spatial and temporal resolution of the dataset relative to the spatial extent and rate of deformation by applying spatial and temporal averaging to reduce phase noise. The method is tested using a Sentinel-1 dataset spanning a tunneling-related subsidence event in the Sri Lankan highlands, showing its ability to reduce data noise and more accurately map the extent and timing of measured subsidence.

Chapter 3 presents a modified algorithm for calculating E-W horizontal and vertical displacements from multiple satellite InSAR datasets and assesses the long-term impacts of tunneling from subsidence through rebound. Previous work tends to focus on surface subsidence during tunneling, but relatively few investigate how the ground recovers from the initial disturbance. Chapter 3 uses a case study to investigate potential non-uniform surface rebound following a known tunneling-induced subsidence

event in downtown Seattle [6]. A modified version of the Minimum Acceleration (MinA) algorithm [16] is used to spatially determine the timing and magnitude of surface rebound after extensive groundwater pumping related to tunnel construction. The accuracy of the modified MinA is assessed by comparing results to a previously published, temporally overlapping InSAR dataset from which E-W and U-D displacements were calculated using the MSBAS method [6].

Chapter 4 presents another modification of the MinA algorithm in which true 3D, i.e., East, North, and Up, displacements are calculated by combining both satellite and airborne InSAR datasets. The method is applied to a case study in which excavation of a new subway station and rail crossover cavern in downtown Los Angeles induced over 1.8 cm of surface settlement as measured by a ground-based monitoring system. This dataset, composed of satellite and airborne SAR data from X, C, and L band sensors, revealed 3D deformation surrounding the 2nd and Broadway subway station and the adjacent rail crossover cavern, with maximum vertical and horizontal deformations reaching 2.5 cm and 1.7 cm, respectively. The analysis shows that airborne SAR data with alternative viewing geometries to traditional polar-orbiting SAR satellites can be used to constrain displacements in the North-South direction while maintaining a good agreement with ground-based data.

The report closes with a final chapter summarizing notable contributions from the research presented in Chapters 2, 3, and 4. The chapter places conclusions from the three research projects into the context of current practice of InSAR time-series analysis for ground subsidence monitoring, and provides recommendations for future investigations.

CHAPTER 2 - 4-D FILTERING OF INSAR PERSISTENT SCATTERERS ELUCIDATES SUBSIDENCE INDUCED BY TUNNEL EXCAVATION IN THE SRI LANKAN HIGHLANDS

2.1 Abstract

During the construction of the Uma Oya Multipurpose Development Project, excavation of a headrace tunnel through highly tectonized metamorphic rock was slowed by repeated major water ingress events. In total, these events resulted in an estimated aquifer depletion of over 9 million m^3, causing widespread surface subsidence. Persistent Scatterer time series analysis of Interferometric Synthetic Aperture Radar (InSAR) scenes acquired by Sentinel-1 between July 28, 2016 and January 1, 2018 has revealed a ~15 km^2 area of subsidence near reported water ingress locations, with a maximum Line of Sight subsidence value of 4.3 cm. A novel 4-D filtering method based on averaging spatial and temporal pixel neighbors was applied to the unwrapped PS pixels, significantly reducing noise from sources that appear randomly in spatial and temporal domains, and increasing the ability to accurately identify the onset of subsidence and track surface volume loss over time. A maximum average subsidence rate of 0.15 mm/day coincides with maximum tunnel discharge measurements, indicating that rock mass consolidation occurred as a result of rapid pore-pressure drawdown within an interconnected discontinuity network and led to fracture closure. The observed subsidence is punctuated by localized maxima and extends in a northwest–southeast orientation, suggesting that the extent of subsidence is governed by previously mapped structural trends of similar orientations. These results highlight the value of the 4-D filtering approach in processing InSAR Persistent Scatterer data to help determine the magnitude and extent of surface subsidence.

2.2 Introduction

The Uma Oya Multipurpose Development Project (UOMDP) began construction in 2014 within the Badulla district of Sri Lanka, and is designed to provide power and irrigation water to local communities. The project consists of two reservoirs connected by a link tunnel, a headrace tunnel, a tailrace tunnel, and a vertical pressure shaft connected to a powerhouse. The 15.3 km long headrace tunnel redirects reservoir water to a 628 m vertical pressure shaft above a hydropower station (Figure 2.1) [21,22]. The headrace and tailrace tunnels were excavated via a 4.3 m diameter double shield Tunnel Boring Machine (TBM). Excavation of the headrace tunnel at depth through heavily fractured, granulite facies metamorphic rock of the Sri Lankan highland complex has led to recurring water ingress during the tunnel boring phase of the UOMDP [21,23]. The largest such event took place between September 2016 to December 2017. During this time, peak water ingress discharge reached nearly 1400 l/s. As a consequence, surface water resources were heavily impacted as hundreds of wells and several streams ran dry [21,24]. Additionally, many buildings were reportedly damaged due to suspected surface subsidence related to aquifer depletion [25].

Large tunneling-induced surface settlements are often observed above deep (>200m) tunnels excavated through fractured crystalline rock [2,3,8,9,26]. Interferometric

Synthetic Aperture Radar (InSAR) is an ideal geodetic tool for detecting, measuring, and monitoring such surface deformation. Satellite data availability has improved dramatically in recent years, which makes InSAR an increasingly viable option for monitoring surface displacements induced by tunneling activities[1–6]. In order to measure surface deformation associated with the UOMDP, an ascending dataset of 33 C-band (λ ~5.6 cm) SAR images acquired by the Sentinel-1 constellation were processed using Persistent Scatterer (PS) time series analysis to determine the extent and magnitude of subsidence surrounding the tunnel axis. In order to further reduce noise present within the dataset, we apply a four-dimensional (4-D) filtering algorithm, similar to that proposed by *Kromer et al.* [27] for point-cloud-based slope monitoring, to the PS time series. This method takes advantage of the high spatial and temporal resolution of the dataset relative to the spatial extent and temporal rate of deformation. After developing a similar method for use with InSAR data specifically, we apply it to our dataset in order to reduce noise and more accurately map the extent and timing of measured subsidence. Application of the 4-D noise reduction algorithm shows the ability to reduce temporally uncorrelated noise within the time series, allowing for more precise identification of the onset, duration, and magnitude of observed surface settlement.

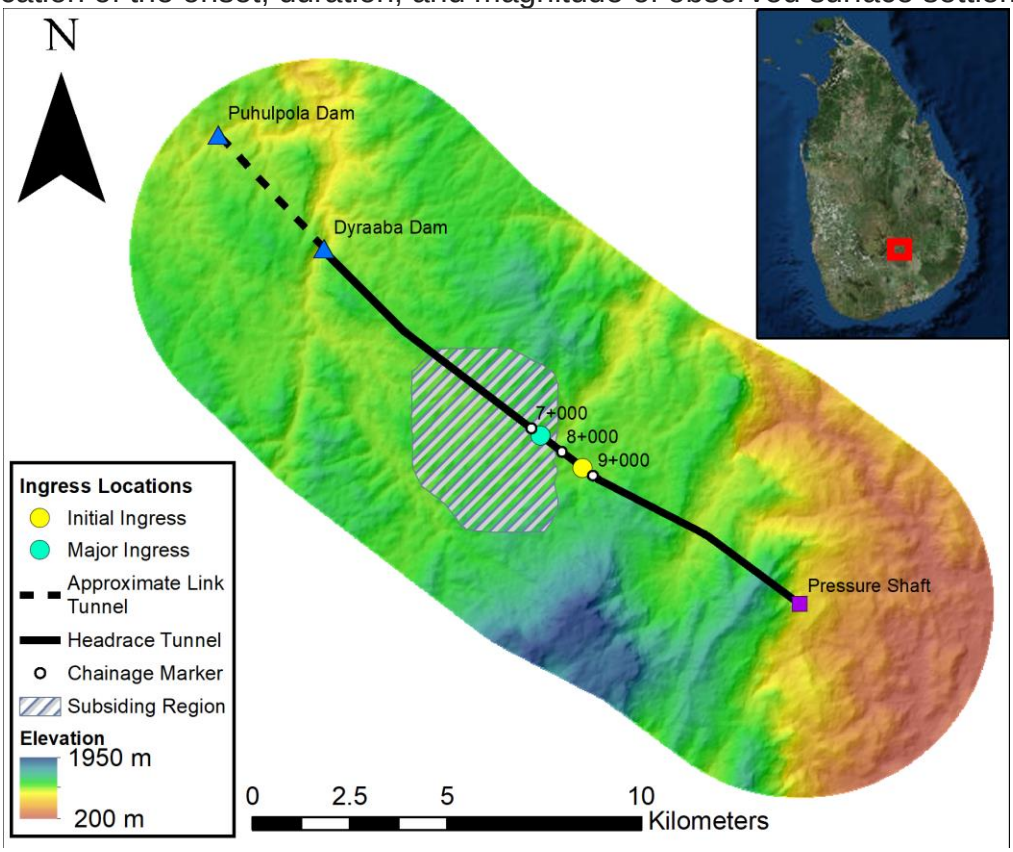

Figure 2.1 Map showing the alignment of the headrace tunnel, as well as the locations of the constructed dams, pressure shaft, major water ingress events, and extent of measured subsidence underlain by a digital elevation model

2.3 Methods

2.3.1 Persistent Scatterer Interferometry

We used repeat pass differential InSAR [11,28] to process 33 ascending SAR scenes acquired between July 2016 and January 2018 by the Sentinel-1 A&B satellites. The GAMMA software [29] was used to create a series of single master interferograms (Figure 2.2) from dual vertically (VV) polarized Single Look Complexes (SLCs), with topographic phase contribution removed via NASA's Shuttle Radar Topography Mission (SRTM) 30 m resolution Digital Elevation Model (DEM). The perpendicular baseline was controlled within 122 m. The master scene was acquired on June 5, 2017, and the maximum temporal baseline is 312 days. After interferogram formation, all data were entered into the MATLAB-based Stanford Method for Persistent Scatterers (StaMPS) software package [13,30]. Persistent Scatterers (PS), defined as pixels that provide stable radar reflections back to the satellite over a time period of interest, were then selected. Unlike amplitude based PS algorithms, StaMPS identifies potential PS through an iterative procedure that estimates phase stability for all pixels in a scene. This is particularly advantageous when applied to natural terrains with rough surfaces that produce low-amplitude reflections, like the highly vegetated Sri Lankan highlands. After input of the single master interferograms, StaMPS identifies a collection of initial PS candidates based on amplitude dispersion values with a chosen threshold of 0.4 [12,13]. Once PS pixel candidates are selected, DEM error is calculated using the relationship between phase and perpendicular baseline. Calculated DEM error is then subtracted by:

$$\mathbf{\Phi_i} - \mathbf{\Phi_\varepsilon} = \mathbf{\Phi_{def}} + \mathbf{\Phi_\alpha} + \mathbf{\Phi'_\varepsilon} + \boldsymbol{n} \qquad (1)$$

where Φ_i is the initial phase, Φ_ε is the DEM error, Φ_{def} is the phase change due to surface deformation, Φ_α is the atmospheric phase contribution, Φ_ε' is the residual DEM error (ideally near zero), and *n* is a random noise component associated with all other sources of error. Since any pixel with random phase has a finite probability of being selected as a PS candidate, final PS pixels are selected by comparing the probability density function of phase stability values from the PS candidate population with that of a population of pixels with random phase. A threshold phase stability value is then selected in order to maximize the number of true PS pixels while keeping the proportion of potentially random pixels below a specific value. For our dataset, an average random pixel density threshold of 20 pixels per km^2 was used. This process iterates until convergence on a statistically robust set of pixels, reducing the impact of temporal decorrelation and improving the signal to noise ratio for each interferogram. Data are then unwrapped within StaMPS using a stepwise 3-D unwrapping algorithm [31].

It is often highly difficult to separate atmospheric phase contributions from the desired deformation signal [32,33]. Tropospheric effects are caused by variations in pressure, temperature, and relative humidity in the lower troposphere, and are capable of obscuring signals of interest [20], especially in tropical areas that experience large fluctuations in tropospheric water vapor density [34] such as Sri Lanka. Because each interferogram contains the same master scene, the atmospheric phase contribution from that scene is present in all interferograms and therefore correlates in space and

time. The atmospheric phase delay from the master scene is estimated and removed in StaMPS using a low-pass filter in the temporal domain. Atmospheric contributions from slave scenes, however, are more difficult to estimate because they do not correlate in time.

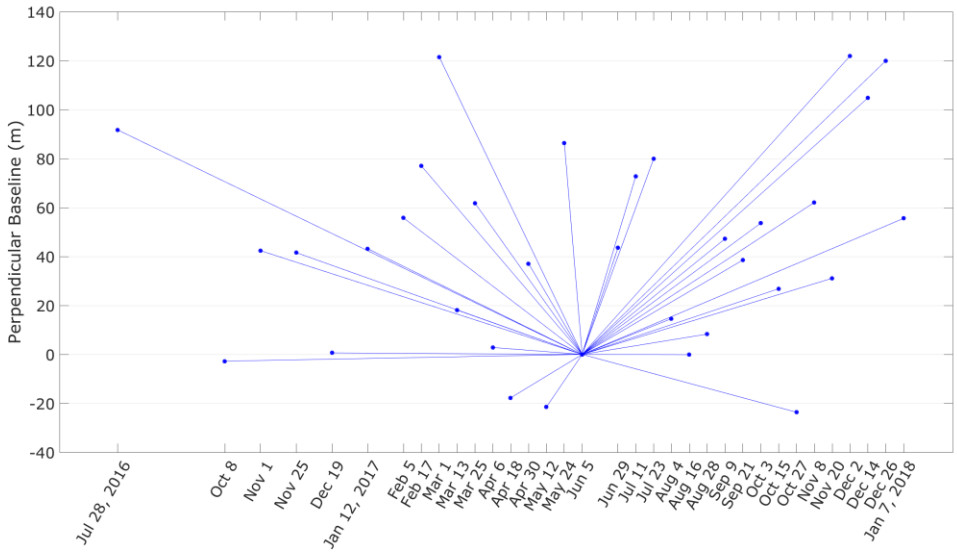

Figure 2.2 Baseline plot of single master interferograms used for StaMPS time series processing

2.3.2 4-D Filtering

After PS processing, significant noise still existed within the data. Random noise can be reduced or filtered through averaging, which is especially useful for datasets with low signal-to-noise ratios. In order to further reduce these error sources, we have modified a 4-D filtering algorithm originally designed for use with terrestrial laser scanner data for rock slope monitoring described by *Kromer et al.* [27]. Since this method employs filters in both temporal and spatial domains, we consider any source of noise that does not correlate in both space and time to be random noise. Specifically, we attempt to reduce noise from sources including temporally uncorrelated atmosphere, residual DEM error, noise from any false positive PS selections, and any errors introduced during phase unwrapping.

For a series of random measurements within an unknown population, regardless of the distribution in which they are sampled, sample means always converge to a Gaussian distribution. Estimation of the population mean occurs by averaging sample means. For data given in a time-series format such as InSAR Persistent Scatterers, each pixel possesses neighbors in both the spatial and temporal domains. Spatial averaging tends to smooth any signal, however, greater averaging in the spatial domain can be advantageous when the spatial extent of deformation is much larger than the neighborhood radius used for averaging. Similarly, averaging along the temporal domain can be applied as long as the temporal averaging window is much smaller than the expected temporal rate of change [27]. In theory, averaging both spatial and

temporal neighbors, as opposed to only using one or the other, has a multiplicative effect in reducing the standard error [27]. This error reduction increases the potential to elucidate signal changes from data with higher levels of random noise.

We used this information to develop a 4-D noise reduction filter and applied it to a time series of PS pixels identified by StaMPS within our study area. Before applying the filter, pixels were masked if their deformation value was zero or greater, indicating no deformation or uplift, during a selected reference scene. This was done to remove stable pixels along the boundary of the subsidence signal of interest. For each pixel, a remaining input radius defined the spatial neighborhood, while the temporal neighborhood used the same pixel location but from equal time intervals before and after the filtered scene. In total, eight equal interval radii and temporal windows were used, ranging from 0 to 210 m and 0 to 84 days, respectively. 12-day intervals were selected based on the repeat time of the Sentinel-1 constellation. Since the degree of surface deformation changes slowly over time, the filter ensures that an equal number of temporal neighbors are used before and after the reference scene. This means no temporal averaging occurs in the first or last scene of the time series because they are missing temporal neighbors in one direction. Therefore, scenes closer to the center of the time series have access to more temporal neighbors than those closer to the beginning or end. The procedure outputs up to 64 different combinations of spatial and temporal filtering for each of the 33 scenes in the PS time series. It is important to note that pixel values are changed based on spatial and temporal averaging, but the positioning of the PS points remain constant, unlike the case in a smoothing polygonal mesh or other filtering methods [27].

Given that up to 64 filtering combinations are available for each scene, it is important to identify the optimum combination of spatial and temporal neighbors for a given scene. The appropriate number of time steps and spatial neighbors will depend on the signal being studied, specifically its spatial extent and temporal rate of change. A high degree of temporal filtering is not advised for studying processes with high temporal variability such as volcanic or earthquake deformation, or in cases where the temporal resolution of the data is limited.

Every combination results in various advantages and disadvantages depending on the amount of noise present in each scene. Combining a high degree of spatial averaging and a low number of temporal neighbors imposes a degree of smoothing, which can allow noisier pixels to propagate within a scene and reduce the ability to resolve the true signal (Figure 2.3). The ideal degree of filtering is identified separately for each scene as the case that minimizes the variance of pixel values in time and space. For each pixel, a spatial neighborhood is established and the variance of all pixels within it is calculated. The spatial variance for each pixel within a scene is then averaged, providing a single variance value. Temporal variance is then calculated for each pixel based on the value of the pixel in the reference scene, as well as the scenes used for temporal filtering. Temporal variances are then averaged into a single value for each scene, then averaged again with the spatial variance value. The filtering combination

that produces the least overall average variance is then selected for each scene in the time series.

2.3.3 Volume Estimation

To better understand the relationship between surface deformation and groundwater depletion, total volume estimates were calculated for comparison. After selection of the final time series, each scene was linearly interpolated to form a complete surface across the subsiding region. These interpolated surfaces were used to calculate total volume losses due to settlement. Groundwater volume loss was then estimated by compiling reported tunnel discharges (n = 8 measurements) from various Sri Lankan newspaper articles and official government reports, then using a step-wise function to determine a minimum estimate of water volume.

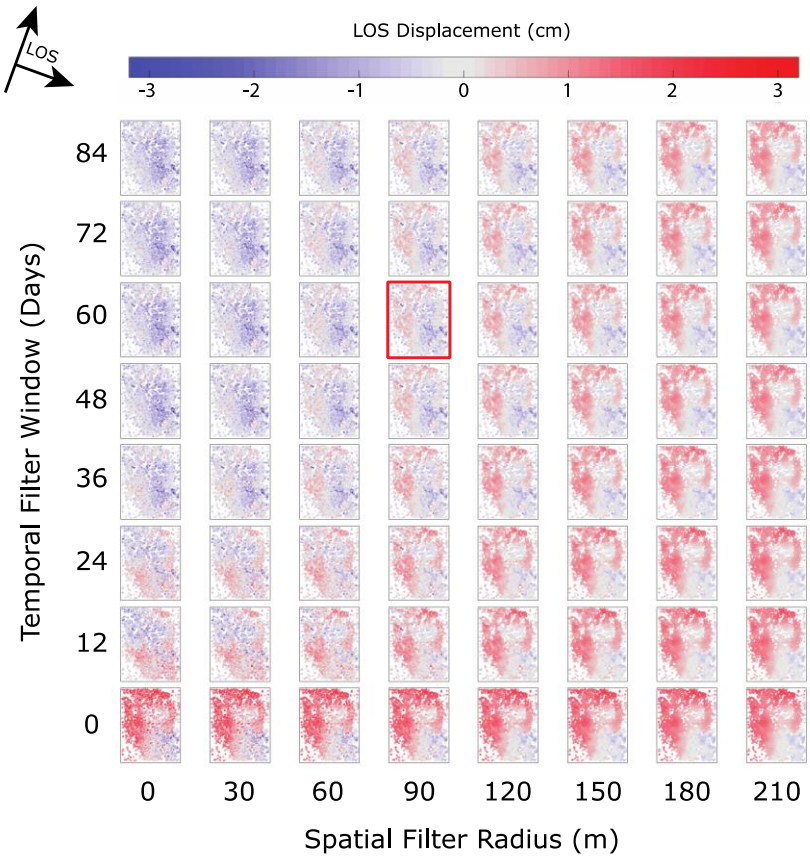

Figure 2.3 Combinations of spatial and temporal filtering for an interferogram with a significant degree of noise. The selected filter combination is represented by the scene highlighted in the red box

2.4 Results

2.4.1 StaMPS Output and Optimal 4-D Filtering

After StaMPS processing and masking with a selected reference scene of November 8, 2016, 3558 PS pixels were selected within our area of interest. It is immediately clear that several scenes contain non-permanent deformation over short time periods (Figure 2.4), most notably between April 6 and May 12, 2017. This is unexpected given that subsurface fluid extraction is usually followed by continuous surface subsidence over short time periods [2,3,6,35,36], and indicates that these scenes contain greater levels of noise. These short term increases in noise are likely due to atmosphere present at the time of the slave acquisition.

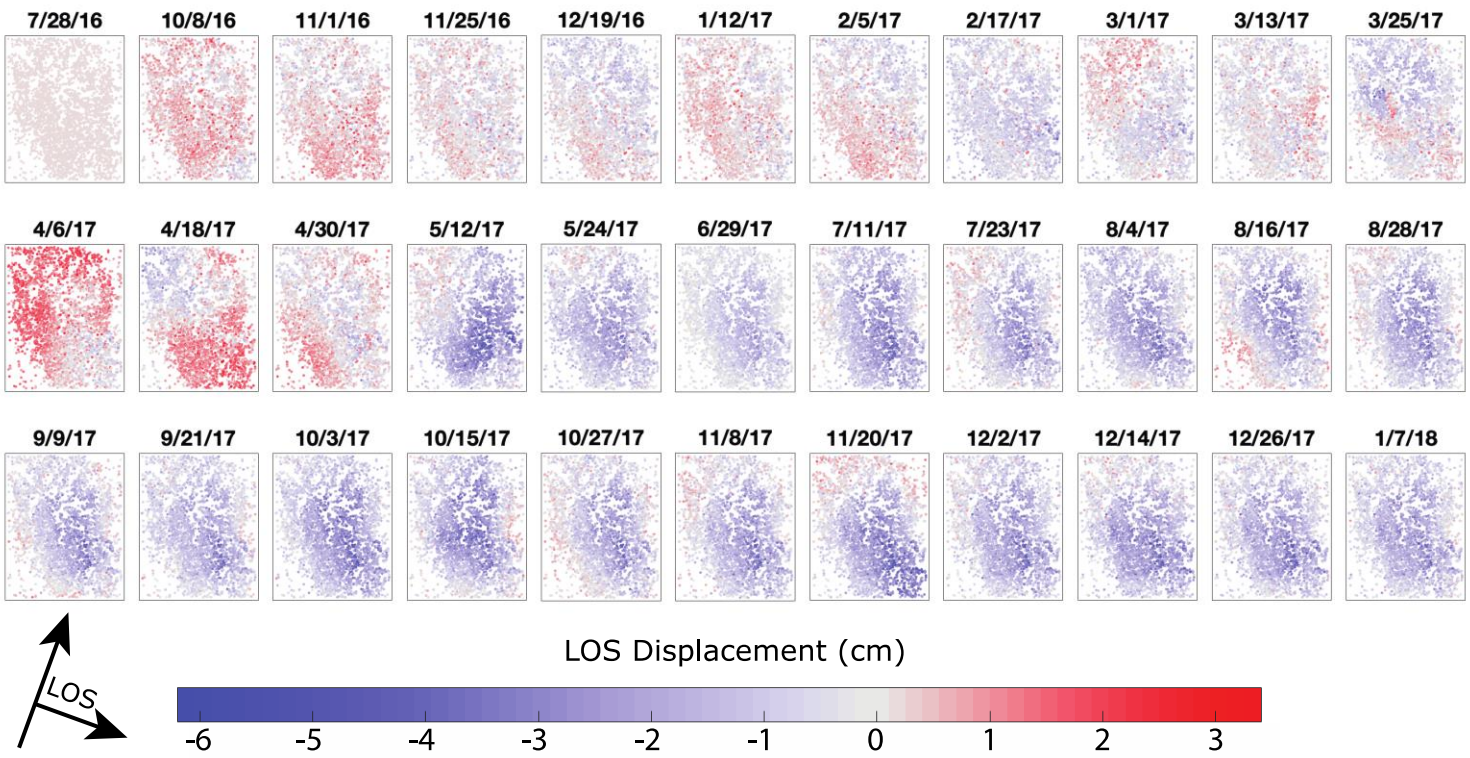

Figure 2.4 StaMPS time series output within the study area

The 4-D filtering method applied to the StaMPS output is designed to reduce noise in the time series by combining spatial and temporal neighbors. The optimum combination of neighbors for each scene were selected based on minimizing overall spatiotemporal variance of the data (Figure 2.5). For all scenes, variance decreased with increasing temporal filtering, however, diminishing improvements were observed with each step up in window size (Figure 2.5). The optimum degree of spatial filtering was found to be more variable. Scenes containing more noise tended to undergo less spatial filtering, while relatively noise-free scenes often incorporated greater spatial filter radii. The degree of spatial and temporal filtering for each acquisition is shown in Table 2.1.

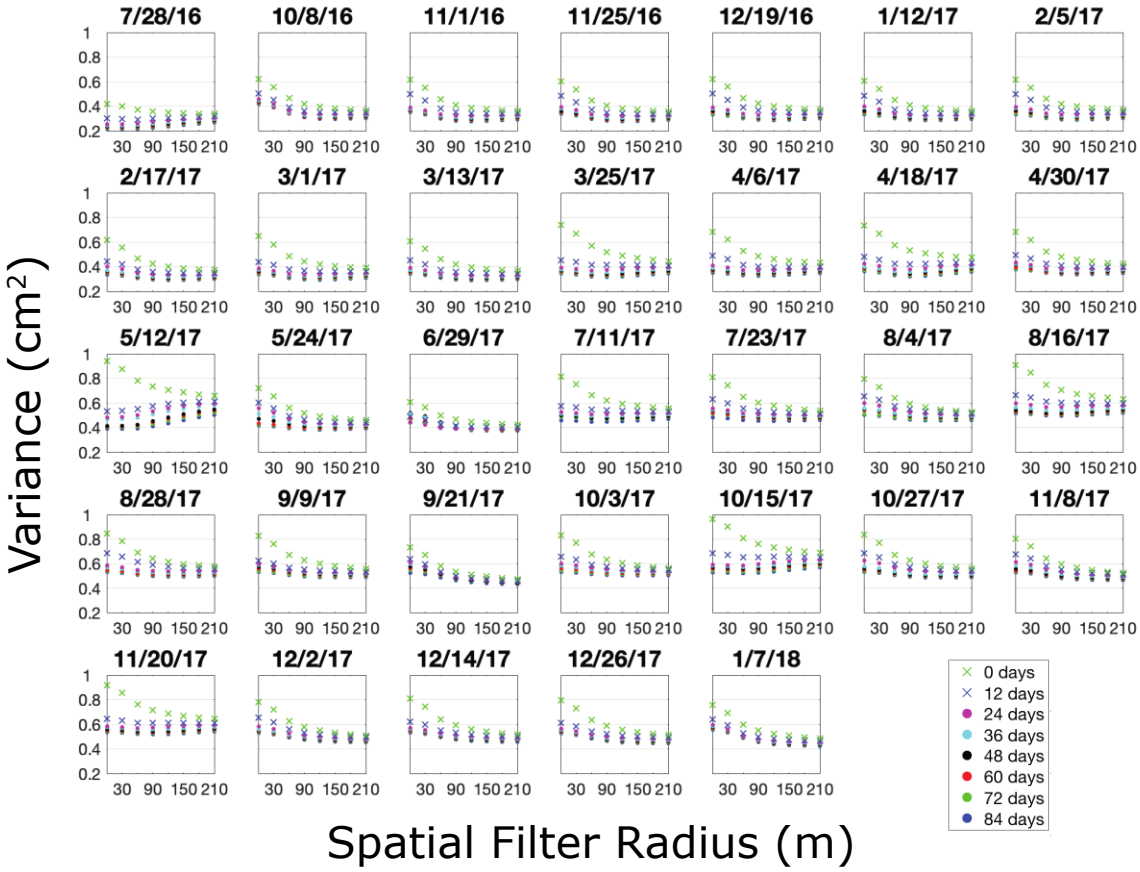

Figure 2.5 Average variance of all 4-D filtering combinations for each interferogram

Table 2.1 Applied spatial and temporal filter sizes

Acquisition Date	Spatial Filter Radius (m)	Number of Temporal Neighbors
7/28/16	30	0
10/8/16	150	0
11/1/16	120	2
11/25/16	120	4
12/19/16	120	6
1/12/17	120	6
2/5/17	120	6
2/17/17	120	8
3/1/17	120	8
3/13/17	120	10
3/25/17	90	10
4/6/17	90	10
4/18/17	90	10
4/30/17	120	10
5/12/17	30	10
5/24/17	120	10
6/29/17	180	10
7/11/17	60	10
7/23/17	120	10
8/4/17	120	10
8/16/17	90	10
8/28/17	120	10
9/9/17	150	12
9/21/17	210	14
10/3/17	150	14
10/15/17	60	14
10/27/17	150	12
11/8/17	210	10
11/20/17	90	8
12/2/17	210	6
12/14/17	210	4
12/26/17	180	2
1/7/18	210	0

2.4.2 Observed Deformation

PS processing combined with 4-D filtering elucidates a pattern of increasing subsidence over the time period of interest (Figure 2.6). Localized Line of Sight (LOS) subsidence is first observed on November 1, 2016 and subsequently expands into a well-defined pseudo-elliptical area spanning ~15 km^2. The magnitude and gradient of LOS subsidence both increase toward the center of the affected area, which forms a settlement trough aligned NNW-SSE (Figure 2.7). From November 1, 2016 to November 20, 2017, a span of 384 days, a maximum total LOS subsidence of 4.3 cm was measured resulting in an average settlement of ~0.1 mm/day. Subsidence rates vary slightly over time, and are seen to have been increasing most rapidly between April 16 and August 4, 2017 when the average reached ~0.15 mm/day (Figure 2.8).

Initial ingress began at some point after August 4, 2016 near chainage marker 8+840, with sustained discharges greater than 400 l/s [24,37]. Inflows increased greatly on April 17, 2017, reaching at least 1200 l/s [25] with some outlets reporting values as high as 1460 l/s [38]. In order to determine a minimum estimate of the total groundwater volume loss over the time period of interest, we estimated discharge values using a step-wise function (Table 2.2). Since no timing constraints were available for peak discharge, the 1070 l/s value reported on June 21, 2017 was used for the maximum discharge. Additionally, a baseflow (i.e. corresponding to zero-subsidence) discharge of 300 l/s is assumed. Integration of the estimated hydrograph above this point results in a total minimum aquifer volume loss of 9.2 million m^3.

2.5 Discussion

2.5.1 Consolidation Mechanism and Timing

Bedrock consolidation processes resulting from excavation-induced groundwater drainage have a history of causing surface settlements [2,3,8,9,26,39]. In fractured crystalline rock, two hydro-mechanically coupled mechanisms are thought to induce surface settlement during drainage events. On shorter timescales, interconnected fracture networks form pathways that allow for rapid water drainage through the rock, which in turn reduces internal pore pressures leading to closure of fractures. The other potential contribution involves the reduction of pore pressure within meso-scale fractures of primarily intact rock blocks, a much slower process expected to take place over several years [8,9].

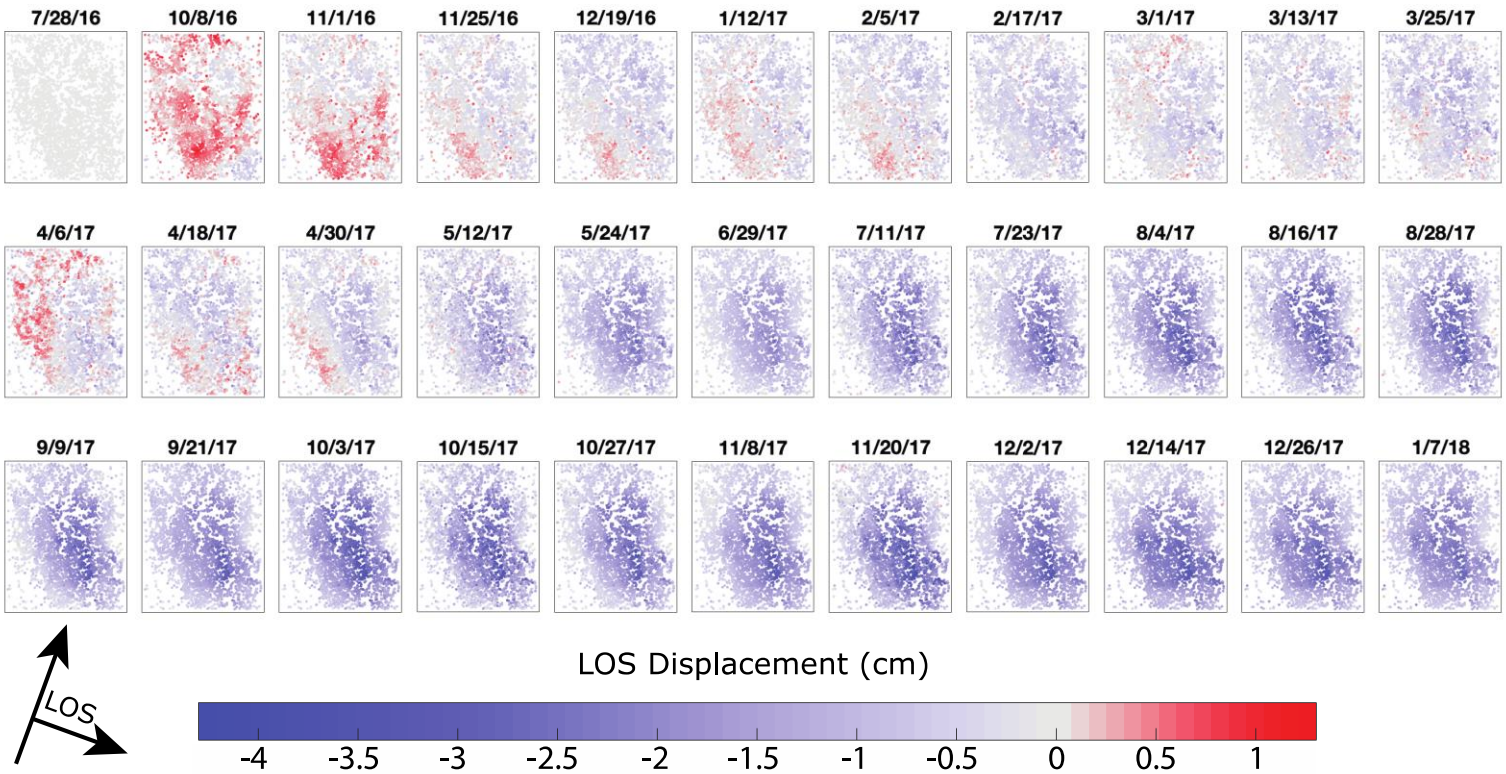

Figure 2.6 Final time series after implementation of 4-D filtering

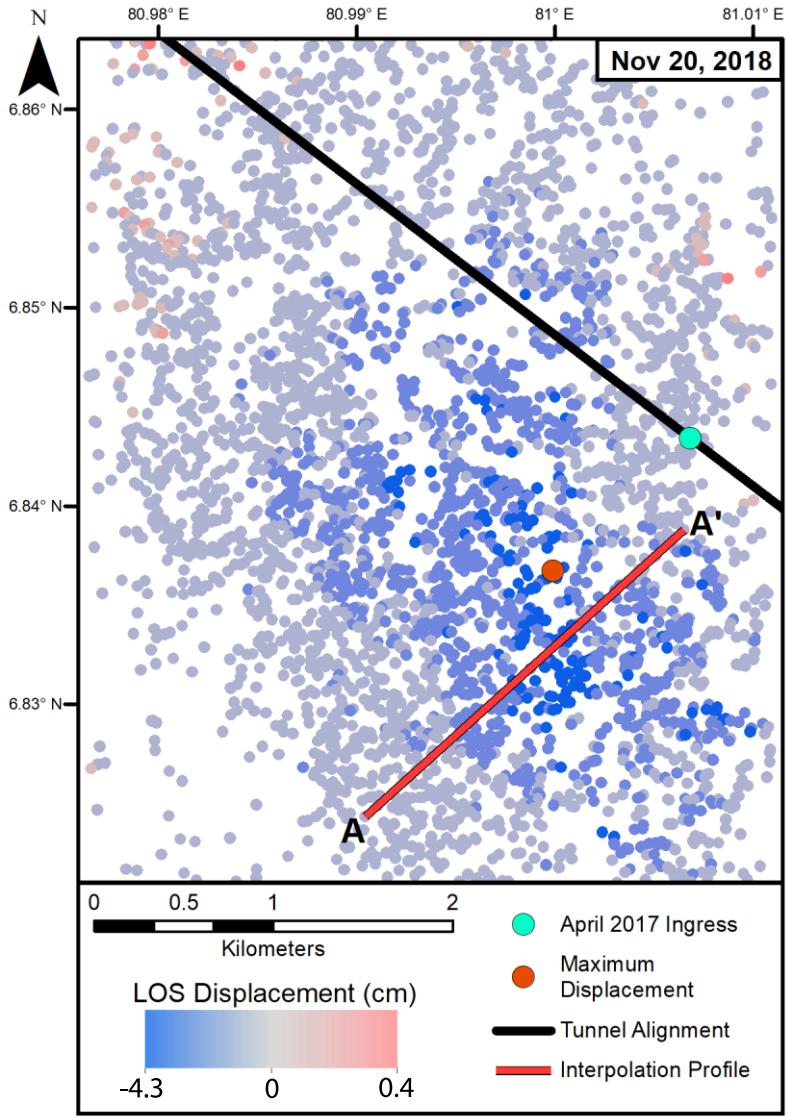

Figure 2.7 Deformation spanning July 28, 2016 to November 20, 2017 highlighting the location of maximum measured LOS subsidence and the tunnel alignment. The profile line shown was used to interpolate displacements shown in Figure 2.8

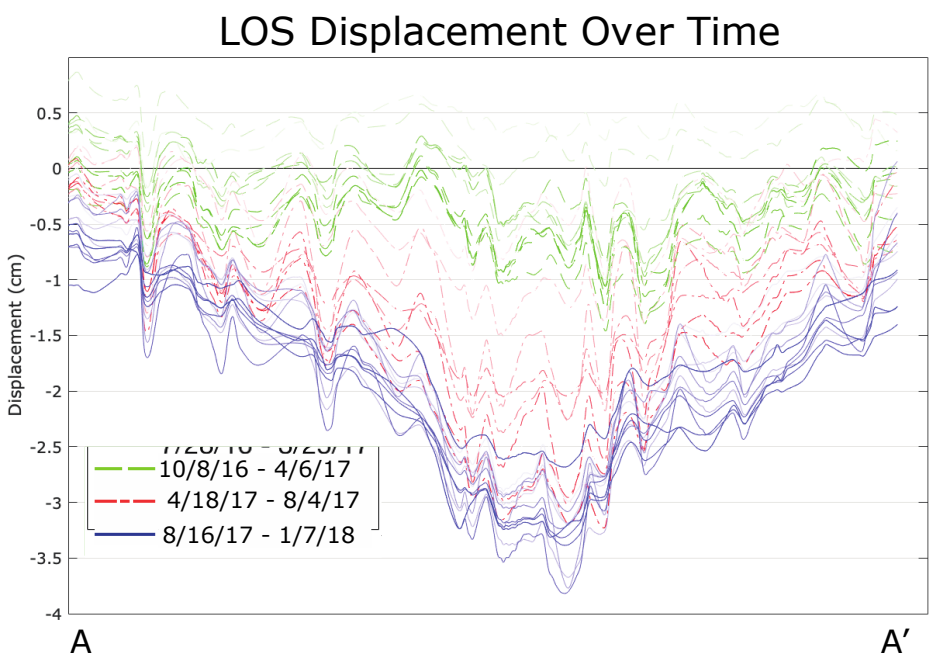

Figure 2.8 Interpolated profile displacements over time

Date	Reported Discharge (l/s)	Source
December 31, 2016	~400	Ismail, 2017
April 17, 2017	1200	Ministry of Mahaweli Development and Environment, 2017
June 21, 2017	1070	Indrajith, 2017; Mudalige, 2017; Wickramasinghe, 2017
June 25, 2017	976	De Silva, 2017
July 2, 2017	850	"Project company promises new houses," 2017
October 22, 2017	583	"Decrease in water leakage," 2017; "Investigations underway into Uma Oya Project leakage," 2017; Silva, 2017
October 23, 2017	400	"Uma Oya seepage," 2017
December 17, 2017	200	Ministry of Mahaweli Development and Environment, 2017; Maloney, 2017

Table 2.2 Discharge values reported by the Sri Lankan government and various media outlets

A lag time between the occurrence of tunnel inflows and the onset of surface subsidence can indicate the primary consolidation mechanism. Best estimates currently available for diffusion times between tunnel and ground surface range between 8 hours to 165 days [9], but are dependent upon the geometry of the fracture network, as well as tunnel depth relative to the water table. Our time series results fall within this range, with surface settlement having begun between October 8 and November 1, 2016, approximately 65 to 89 days after the initial onset of inflows after August 4, 2016. The coincident timing between increased tunnel discharge and increased subsidence rates during the April 2017 major ingress event (Figure 2.9) indicates a direct relationship between aquifer depletion and surface deformation. Additionally, over a centimeter of rebound is measured between November 20, 2017 and January 7, 2018, a time period that coincides with a rapid reduction in tunnel discharge as it returned to baseflow levels. Temporally coincident rapid changes in both discharge and subsidence rates, combined with the fact that subsidence is only observed over a 384-day period, indicate that consolidation processes in this case are dominated by closure of larger faults and fractures as opposed to long term pore pressure reduction within intact rock blocks.

2.5.2 Controls on Extent and Magnitude of Subsidence

Localized maxima are found near the center of the subsiding region, and are elongated in a NNW–SSE orientation similar to the long axis of the observed subsidence bowl. This trend does not directly follow the tunnel alignment, and maximum subsidence is found over 1 km away from the location where the greatest inflow rates were measured, indicating that location of tunnel excavation itself has little influence over the potential maximum extent of surface subsidence during large drainage events.
In hard rock environments, groundwater flow at depth is controlled by the presence of conductive fractures [40]. Previous studies have shown that tunnel inflow rates are controlled by the degree of bedrock fracturing, as opposed to the surrounding lithology or tunnel depth, especially for tunnels excavated at depths greater than 200 m [40]. This seems intuitive, as the greater the degree and persistence of fracturing, the more likely a fracture network will intersect any nearby aquifers. Tunnel excavation for the UOMDP takes place entirely within the Sri Lankan Highland Complex (Figure 2.10), which is composed primarily of highly fractured Pre-Cambrian gneisses [41] with demonstrated potential for hosting large volume water ingress events [23,24]. Surface water resources were significantly impacted around the time peak inflow discharge was reached. This indicates that the bedrock fracture network at depth is interconnected with fractures closer to the surface, allowing for access to both deep and shallow aquifers that are known to exist within the local groundwater regime [21,24]. This created a situation where overlying strata acted as an unconfined aquifer, which then fed through conductive fractures into the tunnel excavation with a head of greater than 200 m.

Predicting water ingress in fractured crystalline rocks presents a difficult task due to the fact that the permeability distribution within fractured crystalline rock is strongly

heterogeneous and can range orders of magnitude [40]. This is evidenced by a change in fracture orientation as the TBM progressed from primarily horizontal to primarily vertical just before the initial onset of water ingress [24]. This indicates that groundwater storage geometry controls the extent of surface settlement, rather than the tunnel location. In most cases, subsurface fluid storage systems including oil, gas, magma, or water reservoirs are controlled by the host rock structure [36]. We suggest that the extent of the NNW–SSE elongated subsidence pattern is likely to be controlled by buried faults that align with previously mapped structural trends in the area [42].

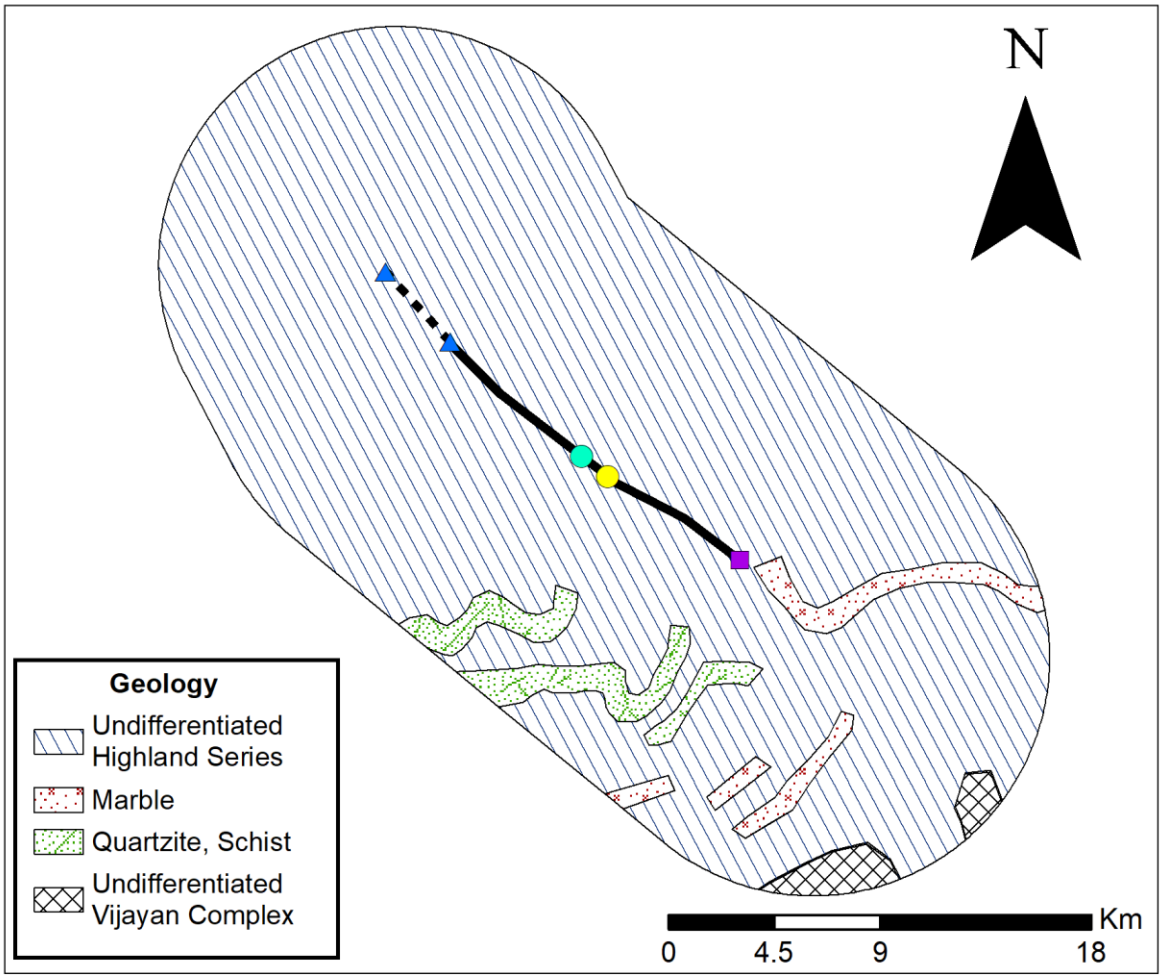

Figure 2.10 Digitized bedrock geology of the study area modified from Cooray

Fracture orientation also plays a major role in controlling the magnitude of observed subsidence. In general, subsidence is relatively insensitive to the closure of vertical discontinuities, because their closure allows for intact rock extension in the horizontal direction, which only generates vertical subsidence through a “Poisson’s ratio” effect [39]. The closure of horizontal joints, however, contributes directly to vertical shortening. Previous Discrete Element numerical modeling results show that varying the normal stiffness of horizontal fractures can produce settlements an order of magnitude greater

than vertical fractures [8]. Knowing that conductive fractures are primarily vertical in the region where water ingress was encountered, this may explain how a total water volume loss of 9.2 million m^3 can produce much smaller surface volume losses. In this case, estimated surface losses of ~250,000 m^3 (Figure 2.11) are ~3% of the total water volume loss.

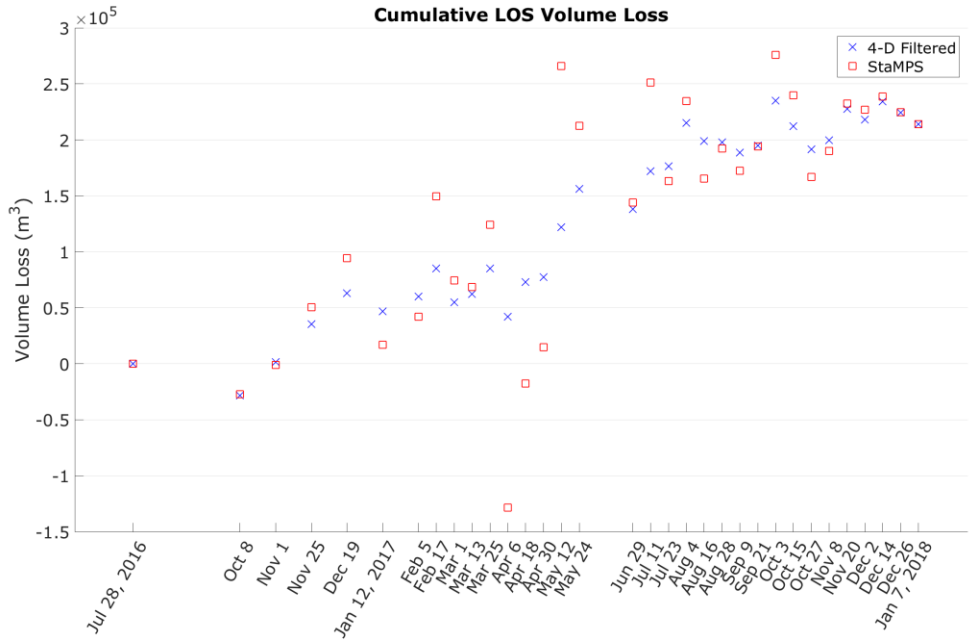

Figure 2.11 Volume loss measured from interpolated surfaces using StaMPS and 4-D filtered time series

2.5.3 4-D Filtering Noise Reduction

Implementation of the 4-D filtering technique clearly demonstrates an ability to reduce noise within the dataset. Improvements in the precision of deformation measurements are attained by averaging neighbors in both spatial and temporal domains, while allowing different neighbor combinations to be used within the time series. Averaging in the spatial domain is useful when the spatial extent of deformation is much larger than the radius used for averaging; in other words, deformation anomalies at scales that are small relative to the filter radius will be undetectable after the filter has been applied. Also, the approach used effectively assumes the deformation within the radius to be symmetrical. In our case, the subsidence trough is observed to deepen at a greater rate closer to the center (Figure 2.8), which may incorrectly decrease pixel values near the trough during spatial filtering. The inclusion of temporal filtering results in a greater ability to resolve smaller deformations and more easily recognize the onset and gradual increase of subsidence, especially for scenes containing higher levels of noise after PS processing (Figure 2.11). This noise is most likely due to turbulent atmosphere, which can cause either a phase increase or decrease depending upon the degree of atmospheric delay present in the master scene relative to that of the slave scenes. It is therefore necessary to select a master scene with an average degree of atmospheric delay for time series processing such that atmospheric errors in the results do not

strongly correlate through time. The majority of noise reduction occurs within the first few temporal window sizes, with diminishing returns thereafter.

When choosing whether to apply a temporal filter, one must take into account the rate of deformation and the temporal resolution of the data. InSAR acquisition rates, limited by the repeat cycle of the satellite constellation, must be high compared to the rate of deformation. This requires a temporal resolution such that the amount of deformation between scene acquisitions is less than the detection limit of the sensor. Satellite InSAR detection limits vary based on surface scattering properties, but are usually on the order of several millimeters for C-band sensors [11]. Assuming a detection limit of 3 mm, average deformation rates should not exceed 0.125 mm/day during the time period in which our temporal resolution is 24 days (October 8, 2016 to February 5, 2017) and should not exceed 0.25 mm/day when acquisitions are made every 12 days (after February 5, 2017). An overall average rate of 0.1 mm/day and a maximum sustained rate of 0.15 mm/day are therefore within our limits for observable deformations. If deformation rates exceed detection limits, the application of a temporal filter may create the appearance of artificially reduced deformation rates.

2.6 Conclusions

Satellite InSAR analysis revealed development of a ~15 km^2 patch of subsidence near water ingress locations along the headrace tunnel of the UOMDP between October 1, 2016 and November 20, 2017. StaMPS software was used to identify a dense set of over 3500 PS pixels within the highly vegetated area at surface above the tunnel alignment. A novel 4-D filtering method applied to the unwrapped PS pixels significantly reduced noise from sources that appear randomly in space and time, increasing our ability to accurately identify the onset of subsidence and measure surface volume loss over time. A maximum average subsidence rate of 0.15 mm/day coincides with maximum water discharge measurements from the tunnel, which indicates that the primary consolidation mechanism is a result of pressure reduction following groundwater drainage and subsequent closure of larger conductive fractures. The observed subsidence bowl is punctuated by localized maxima and extends in a NW–SE orientation, suggesting that the extent of subsidence is governed by previously mapped structural trends of similar orientation. These results highlight the potential for use of InSAR as a monitoring tool to determine the onset and potential extent of surface subsidence to quickly identify areas at risk of experiencing settlements.

The applied 4-D filtering method is ideal for relatively slow, constant surface deformation. Ultimately, the wavelength of the sensor and the temporal resolution of the dataset determine the maximum deformation rates for which the 4-D filtering technique can be applied. Acquisition rates can be well constrained when using ground-based or airborne SAR methods, however satellite InSAR systems are limited by their polar orbit repeat cycles. This makes data from relatively low repeat time satellite constellations such as Sentinel-1, COSMO-SkyMed, and the future RADARSAT Constellation Mission potentially favorable options for 4-D filtering.

2.7 Acknowledgements

We thank the two anonymous reviewers for their thorough comments that helped improve this manuscript. This work was supported by the University Transportation Center for Underground Transportation Infrastructure (UTC-UTI) at the Colorado School of Mines for funding this research under Grant No. 69A3551747118 from the U.S. Department of Transportation (DOT). The opinions expressed in this paper are those of the authors and not the DOT. The digital geologic map of Sri Lanka was prepared by Aaron Engers, Julia Payne, Jarred Dull, and Bias Adibrata at the Colorado School of Mines.

CHAPTER 3 - TUNNELING-INDUCED RAPID DIFFERENTIAL GROUND REBOUND AND DELAYED SUBSIDENCE IN AN URBAN ENVIRONMENT

3.1 Abstract

During the excavation of the Alaskan Way Viaduct replacement tunnel in Seattle, Washington, USA, a 17.5 m diameter tunnel boring machine nicknamed “Big Bertha” was damaged after encountering unexpected ground conditions. Significant dewatering of multiple aquifers was required to reach the tunnel boring machine for repairs. Groundwater drawdown and soil consolidation associated with dewatering created a 0.4 km^2 region of subsidence in downtown Seattle with vertical settlements exceeding 3.5 cm. Here, we investigate how a subsided urban landscape with complex and poorly constrained geologic and hydrologic conditions responded to a single temporally confined dewatering event. The rate, duration, spatial extent, and magnitude of dewatering-induced displacements are calculated by combining three paths of Sentinel-1 Interferometric Synthetic Aperture Radar (InSAR) data into a time series of vertical surface deformation using the Minimum Acceleration (MinA) algorithm. Data show that post-dewatering rebound within this complex hydrogeologic system occurred at faster rates and with greater spatial variability than initial subsidence, resulting in hazardous differential rebound magnitudes across short distances. Prolonged groundwater pumping at depths greater than 60 m appears to have induced delayed subsidence over a larger area, lasting for over three years after the cessation of pumping.

3.2 Introduction

Subsurface excavations often encounter saturated soils, especially in coastal areas with shallow water tables. When groundwater cannot feasibly be diverted by physical barriers (e.g., sheet piles or ground freezing), underground construction projects commonly use dewatering wells to lower the groundwater table temporarily. Groundwater pumping reduces pore pressure and increases effective stress within subsurface strata, subsequently inducing subsidence in compressible geology [43]. Dewatering for excavation creates artificial and often highly dynamic groundwater systems [44], especially when working in naturally complex geologic and hydrologic conditions. In urban settings, subsidence poses a significant hazard to overlying infrastructure when it occurs non-uniformly over short distances, resulting in differential settlement. Less often considered are potential hazards induced by post-dewatering rebound, and never before have they been studied with detailed spatial geodetic data in an urban setting.

Groundwater monitoring techniques generally rely on borehole networks to measure spatial and temporal changes in groundwater levels. However, borehole-based monitoring networks provide sparsely distributed point information, which can be insufficient to characterize changes in the groundwater regime accurately in complicated subsurface settings. The effects of groundwater changes with respect to surface deformation have been well documented using InSAR at both regional scales [35,45–51] and for individual construction projects [2,3,6,52–55]. Studies have shown that groundwater recharge can cause surface uplift, the duration of which depends on

factors such as geology, degree of aquifer depletion, and groundwater pumping rates [35,50,56,57].

To understand how drained soils spatially respond to recharging in an urban environment, we calculate surface deformation in downtown Seattle (Figure 3.1) over a 5-year period from 2014 to 2019, during which a network of dewatering wells at multiple depths was sequentially initiated and decommissioned. This quantitative assessment of post-dewatering rebound identifies potential hazards associated with a short-term rapid ground rebound, and shows the complex long-term surficial response of multiple deforming aquifers and aquitards within an artificially perturbed groundwater regime.

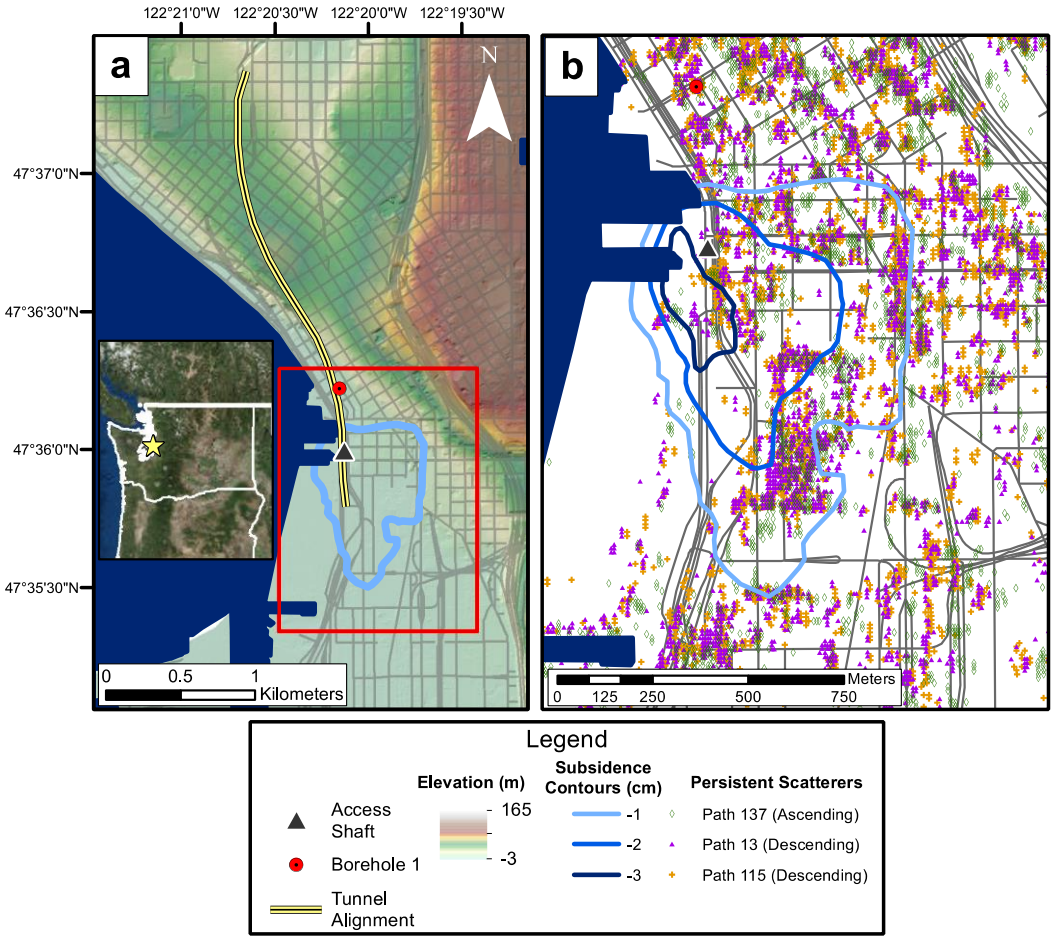

Figure 3.1 a) Location and elevation of the study area, access shaft, and borehole 1. b) Contours of subsidence previously measured by *Samsonov et al. 2016* and persistent scatterer locations of Sentinel-1 data

3.3 Background

3.3.1 Geology and hydrogeology

The greater Seattle area is built on successive glacial, fluvial, and lacustrine deposits truncated by unconformities and deformed through faulting and folding due to a complicated geomorphic and tectonic history [58]. Postglacial bog and recessional lake deposits frequently contain highly compressible peat and organic-rich salt deposits, which are found in locations throughout Seattle [6,58,59]. Many peat deposits in the area are now covered by fill and occur as discontinuous lenses, in which case mapping is not plausible. Subsurface materials show significant variability in spatial extent and thickness, leading to a complicated groundwater regime.

At least two aquifers are known to exist beneath Pioneer Square and surrounding areas in downtown Seattle: an unconfined aquifer within surficial deposits and a confined aquifer composed primarily of sand and gravel [6,60,61]. These aquifers are separated by an aquitard layer composed of cohesive clay and silt that can be found at multiple depths from 3 to 65 m below the surface that range from 1 to 30 m in thickness [60]. Data from the deepest borehole available within the study area (Table 3.1) provide a generalization of the aquifer system. The maximum depths of the confined aquifer are poorly constrained. Regional groundwater studies indicate a confining depth of at least 245 m, while the thickness of unconsolidated deposits composing the Puget Sound aquifer system could reach up to 730 m or more in the downtown Seattle area [59,61].

Table 3.1 Layer data from borehole 1

Top Depth (m)	Bottom Depth (m)	Description	Layer Type
0	7.0	Loose to medium dense, gray-brown, clayey, silty fine sand with wood and concrete debris	Fill
7.0	8.8	Very dense, gray, slightly silty fine sand	Unconfined Aquifer
8.8	16.5	Very dense, gray, silty, gravelly, fine sand	Unconfined Aquifer
16.5	23.5	Very dense, gray, clayey, sandy, fine to coarse gravel	Unconfined Aquifer
23.5	46.6	Hard, gray, silty clay with occasional gravel	Aquitard
46.6	65.8	Very dense, gray, silty, gravelly, fine to coarse sand	Confined Aquifer
65.8	122.0	Very dense, gray, silty, sandy, fine gravel and silty, gravelly, fine to coarse sand with occasional cobbles	Confined Aquifer

3.3.2 Dewatering timeline and initial subsidence

A 37 m deep access shaft was constructed from October 2014 through January 2015 to reach the damaged tunnel boring machine (Figures 1 and 2). A series of dewatering wells were installed to lower the groundwater table to excavate the access shaft and gain access to the tunnel boring machine [6,60,62,63]. A total of fifteen dewatering wells

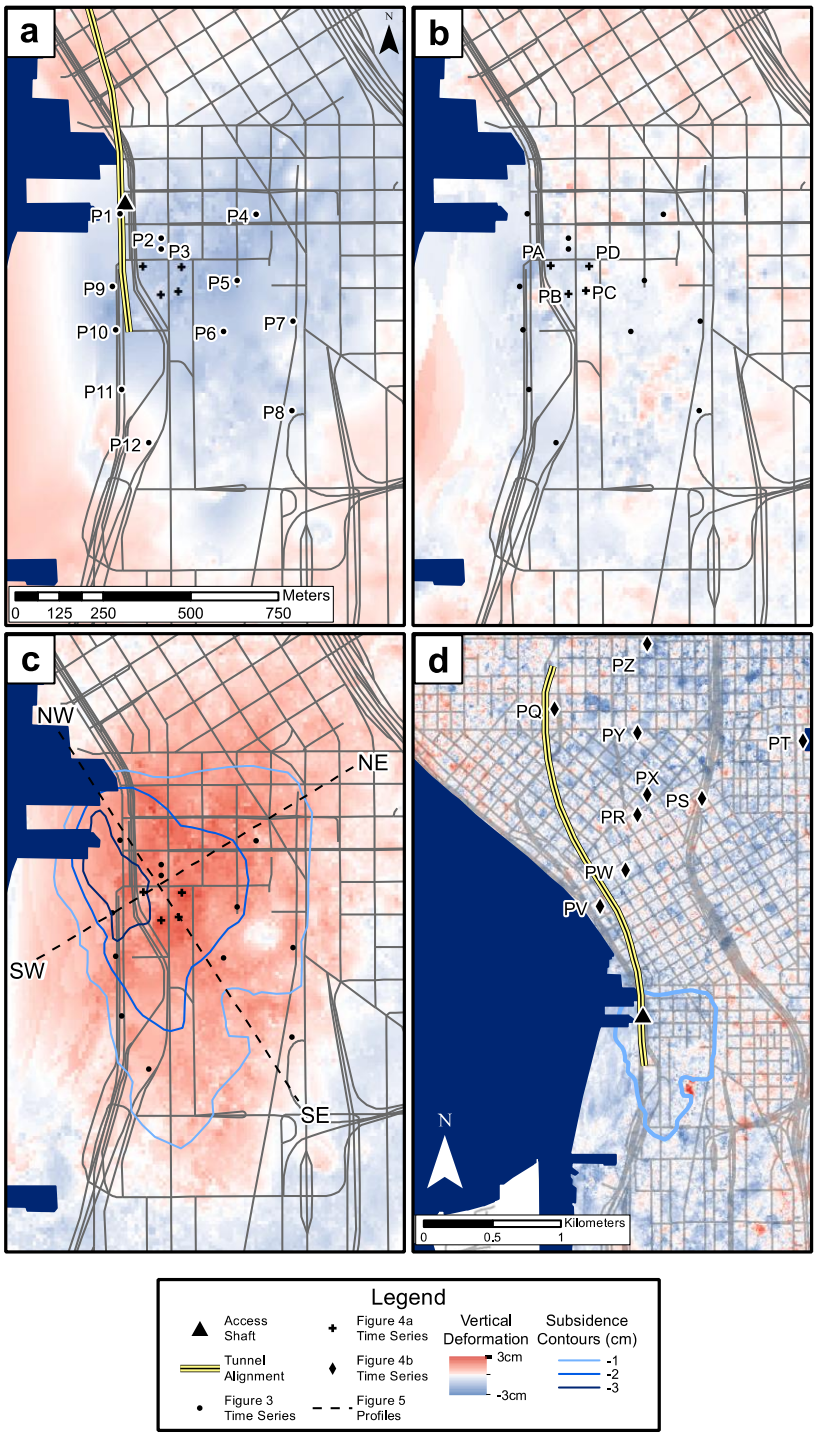

were installed in and immediately around the access shaft, and screened at multiple depths to 61 m to dewater both

Figure 3.2 a) Vertical deformation spanning November 6, 2014 to February 22, 2015. Time series of numbered points shown in Figure 3.3. b) Vertical deformation spanning February 22, 2015 to January 12, 2016. Time series of lettered points PA-PD shown in Figure 3.4a. c) Vertical deformation spanning January 12 to August 5, 2016. Subsidence contours represent deformation from August 31, 2014 to August 26, 2015. Profiles shown in Figure 3.5. 1d) Vertical deformation spanning August 5, 2016 to July 27, 2019. Time series of lettered points PV-PZ shown in Figure 3.4b.

unconfined and confined aquifers. Four internal access shaft wells screened to 46 m began collectively pumping 55 to 110 m^3/day on October 2, 2014. By October 29, seven other shallow wells installed around the outside of the shaft were pumping a total of 320 to 650 m^3/day. Four deep wells (61 m depth) began pumping on November 8 at a combined rate of 3500 to 4100 m^3/day [60,64]. Within two months of the initiation of the deep well pumping, piezometric elevation recorded at a 115 m deep steam plant well located ~850 m northwest of the access shaft fell by over 7.5 m [60]. The wells within the access shaft were shut off by February 19, 2015, while the remaining shallow wells and all deep wells continued pumping until they were sequentially shut off from January 22 to January 24, 2016 [65].

Dewatering and subsequent consolidation were shown to directly cause the formation of an elliptical subsidence feature in downtown Seattle, reaching approximately 0.4 km^2 in size. Previously published RADARSAT-2 spotlight data processed via the multidimensional small baseline subset (MSBAS) technique [15] measured vertical deformation reaching a maximum of 3.5 cm between August 2014 and August 2015, with maximum subsidence rates of 10 cm/yr occurring between August 31 and December 29, 2014 [6,66]. Damaged utilities as a result of this event include a 400 m stretch of 20-inch diameter water line piping beginning 200 m north of the access shaft location [64].

3.4 Methods

Measurements of ground deformation associated with dewatering near the access shaft were acquired by processing one ascending path (137) and two descending paths (115 & 13) of Sentinel-1 data. All available acquisitions before October 19, 2019, were used (Table 3.2). These images have a spatial range and azimuth resolution of 2.3x14 m, and were processed using repeat pass differential interferometry [7,10,11]. GAMMA software [29] was used to create a series of single master interferograms from dual vertically (VV) polarized Single Look Complexes (SLCs). A single master date was chosen for each data path and slave images were co-registered to the geometry of the chosen master scenes, with topographic phase contribution removed via the 3D Elevation Program (3DEP) 1/9 arc-second resolution Digital Elevation Model (DEM, http://nationalmap.gov).

GAMMA's Interferometric Point Target Analysis (IPTA) was used to create a time-series of Persistent Scatterer (PS) pixels. PS pixels were identified using the Mean to Standard-deviation Ratio (MSR) of the radar intensity backscatter. A threshold MSR

value of 1.1 was used to select pixels with low temporal variability, high-intensity backscatters that provide stable phase returns over the time period of interest. SLC values at PS pixel locations were extracted and written to a point data stack. Initial differential interferograms were formed, then analyzed in the temporal domain to measure the linear dependence between the perpendicular baseline and phase for each PS pixel, which was used to calculate DEM corrections. These corrections were subsequently used to update perpendicular baseline values. Linear deformation rates were then calculated for each pixel. The residual phase, considered as a deviation from the linear rate, is composed of atmospheric contamination, baseline measurement errors, any non-linear deformation, and random noise. Since the atmospheric phase contribution from the master scene correlates in space and time, it was extracted using a low-pass temporal filter of the residual phase, then removed from all interferograms. The process was then iterated using the corrected DEM, updated perpendicular baselines, and atmosphere-corrected interferograms. Final deformation values were produced via a phase unwrapping algorithm based on minimum cost flow techniques applied to a Delaunay triangular network.

Table 3.2 Input Sentinel-1 data

Path	Time Span	Master Date	Maximum Perpendicular Baseline (m)	Line of Sight Azimuth	Incidence Angle	Number of Scenes
115	20141106-20191017	20170909	155.1	285°	44°	100
137	20150107-20191019	20170911	129.7	76°	39°	83
13	20150603-20191010	20170914	149.5	285°	39°	92

After LOS deformation time series were constructed for all input datasets, PS pixels (Figure 3.1b) were interpolated to a 10m gridded surface and combined in a post-processing stage using the Minimum Acceleration (MinA) algorithm [16] to estimate vertical and East-West horizontal deformation from multiple LOS time series with high temporal resolution [17,18]. Many InSAR sensors are side-looking systems onboard satellites traveling along polar orbits, preventing LOS measurements outside of a primarily E-W plane and obscuring horizontal deformation in the N-S direction [67]. Because of this low sensitivity, we consider N-S deformation to be negligible. Input LOS displacement time-series were connected to the unknown 2-D velocities among consecutive time acquisitions, creating a system of underdetermined independent linear equations that were solved in the least squares sense by using first-order Tikhonov regularization. Regularization was achieved by imposing constraints to minimize the acceleration of displacements between acquisitions. Once estimated, the displacement velocities were independently time-integrated to extract a single deformation time series.

To assess algorithm accuracy, results from the Sentinel-1 MinA algorithm output were compared with previously published, temporally overlapping RADARSAT-2 vertical displacement data calculated using the MSBAS algorithm [6,15]. As the MSBAS approach consists of generating and simultaneously processing a full sequence of multiple-platform differential SAR interferograms, the primary difference between the algorithms lies in the fact that the MinA approach is a post-processing step in which completed LOS time series are used as inputs.

3.5 Results

3.5.1 Continued subsidence and rebound

The first available Sentinel-1 image for the area of interest was acquired on November 6, 2014, months after the initiation of subsidence, but before the deep wells began pumping on November 8. During the time period in which all dewatering wells were active, widespread subsidence was observed throughout the Pioneer Square area (Figures 3.2a and 3.3). In February 2015, subsidence rates decreased coincidentally with the shutoff of the four wells installed within the access shaft on February 19 (Figure 3.4a). Vertical deformation during this time period shows continued subsidence with scattered patches of uplift (Figure 3.2b). After the 8 remaining wells ceased pumping by January 24, 2016, the immediate widespread rebound was observed across the study area (Figure 3.2c). A maximum total rebound of nearly 3 cm was observed at point PD between January 12 and August 5, 2016, with a maximum uplift rate of 17 cm/yr sustained from January 29 through March 14. Rebound varied greatly over short distances during this time period, with differential rebound magnitudes exceeding 2 cm between points PA and PB in the months after deep wells stopped operating (Figure 3.4a).

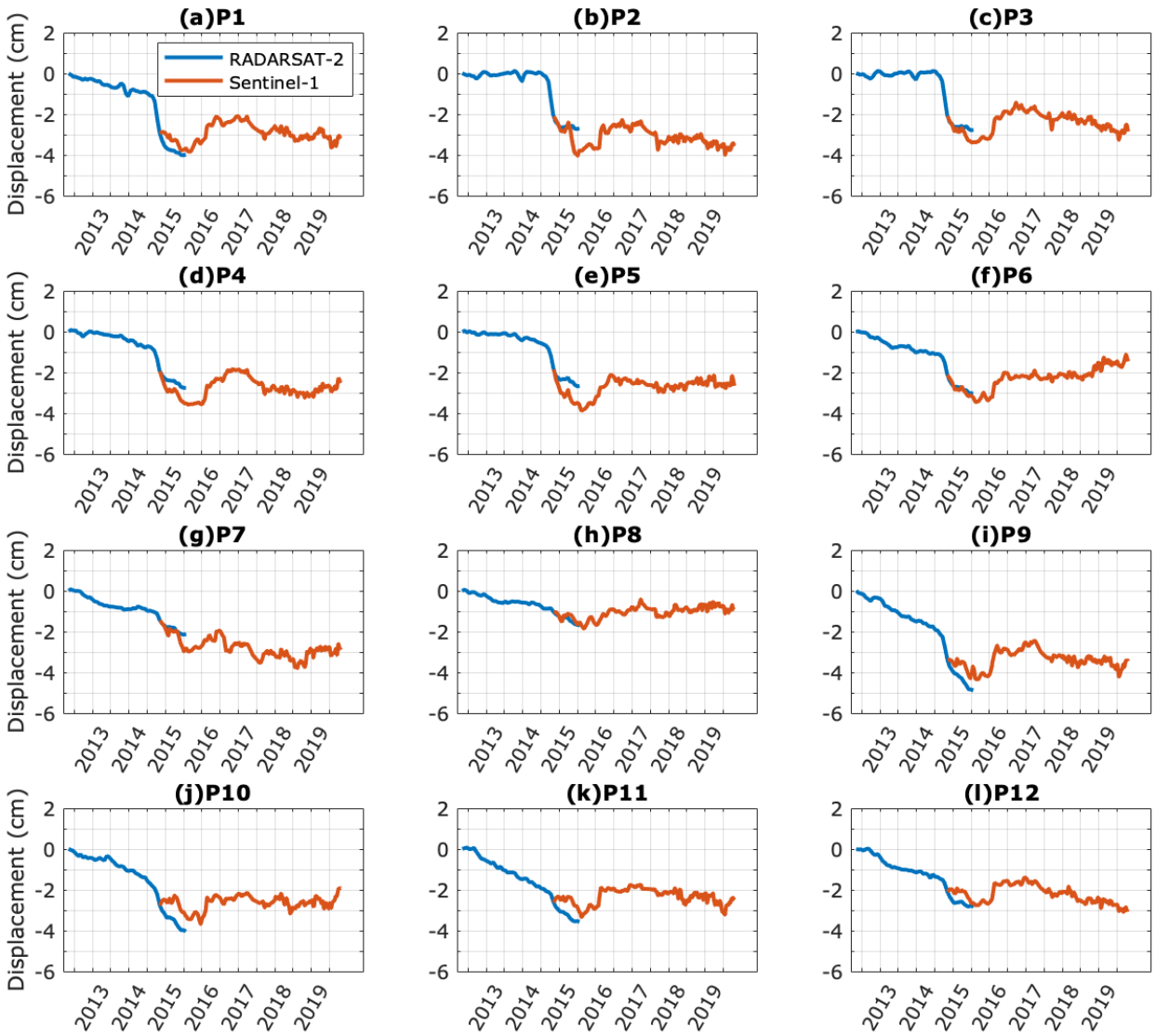

Figure 3.3 Vertical deformation time series of numbered points shown in Figure 3.2a. Data span June 6, 2012 to October 19, 2019. RADARSAT-2 data from *Samsonov et al. 2016.*

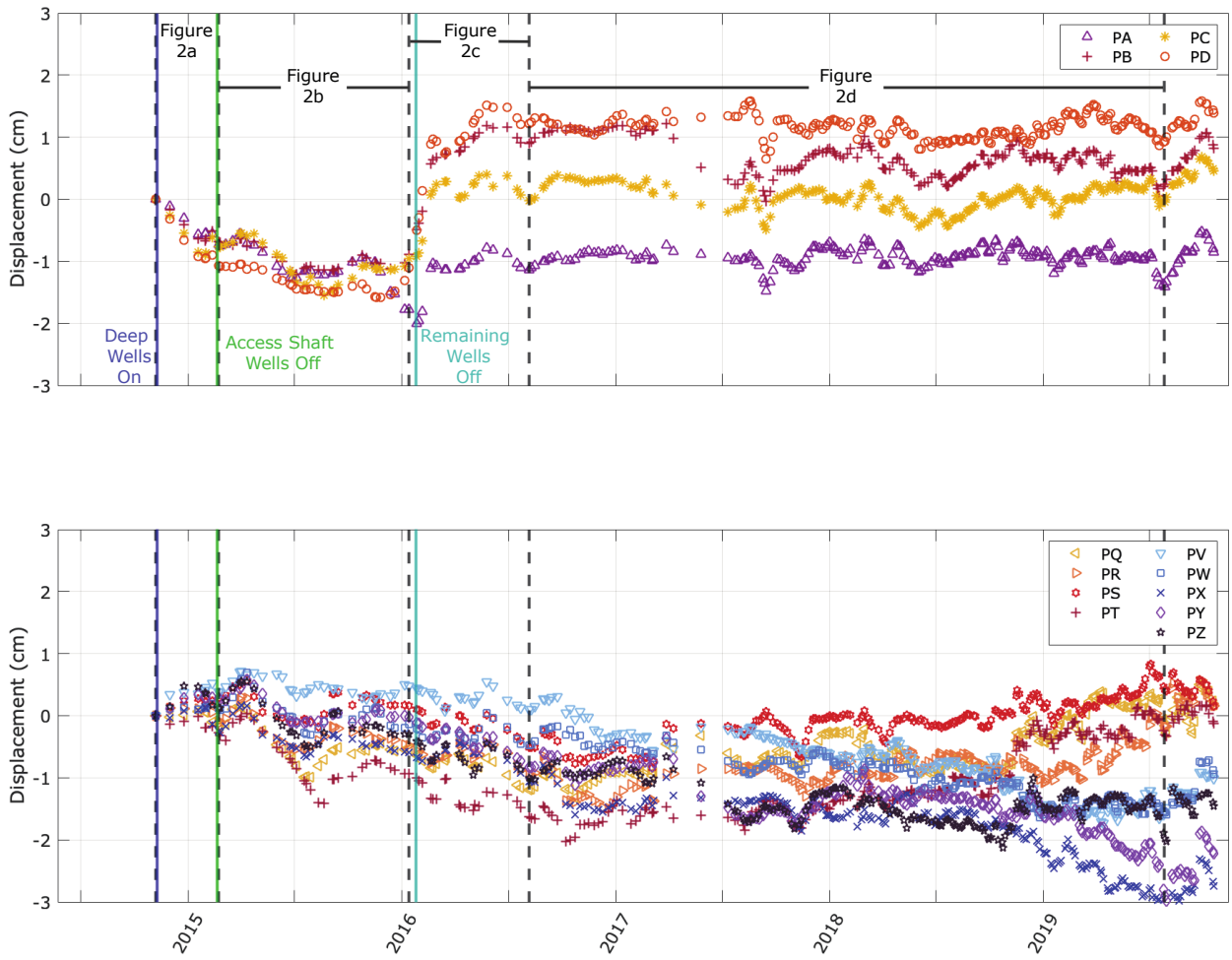

Figure 3.4 a) Vertical deformation time series of points PA-PD shown in Figure 3.2b. b) Vertical deformation time series of points PV-PZ shown in Figure 3.2d

3.5.2 Delayed subsidence

In the months after the deepest wells began pumping over 3500 m^3/day, areas outside of the initial subsidence event also begin to subside. This post-rebound, delayed subsidence was far more widespread than the initial subsidence event, encompassing an area greater than 6 km^2 (Figure 3.2d). The subsided region includes the steam plant, located at point PV, where piezometric elevation in a 115 m deep well decreased by 7.5 m in the weeks following the onset of deep well pumping. Despite the rapid piezometric response, subsidence at the steam plant was not observed until April 2015 (Figure 3.4b), five months after deep well pumping began. From April 10, 2015 to April 9, 2019, point PV subsided a total of 2.4 cm at an average rate of 0.6 cm/yr. Points PX-PZ are all observed to reach a maximum settlement before immediately rebounding by

approximately 1 cm. The timing of the rebound is not uniform, as point PZ reaches maximum settlement on October 23, 2018 while points PX and PY continue to subside until July 29, 2019. Points PQ-PT begin subsiding at similar times and rates to points PV-PZ, but reach maximum subsidence sooner, as early as October 2016. While points PV-PZ continue subsiding, points PQ-PT begin rebounding in late 2018 and 2019, making a full recovery to their original elevations.

3.6 Discussion

3.6.1 Data comparison

Vertical displacements calculated from Sentinel-1 data using the MinA algorithm are generally very similar to those calculated from RADARSAT-2 spotlight data (Figure 3.3) using the MSBAS algorithm [6]. Datasets from both RADARSAT-2 and Sentinel-1 possess C-band sensor wavelengths (~5.5 cm); however, the RADARSAT-2 spotlight data possess a greater spatial resolution (1.6 x 0.8 m) than that of the Sentinel-1 data (2.3 x 14.1 m). The spatial resolution of InSAR data determines the area over which reflecting objects, or scatterers, can be identified. Therefore a finer spatial resolution can potentially identify scatterers that coarser resolutions may not, creating the potential for two datasets of the same wavelength to measure reflections from different scatterers that do not necessarily exhibit the exact same deformation pattern. Despite the use of separate input datasets, the small differences in deformation output indicate that the MinA and MSBAS algorithms are comparable in terms of the ability to extract vertical deformations from combined ascending and descending InSAR data. Additional analyses using unsupervised self-organizing map machine learning algorithms [68] could also be used to assess uncertainty between the RADARSAT-2 and Sentinel-1 datasets.

3.6.2 Deformation

An analysis of post-subsidence surface deformation in downtown Seattle reveals complex hydro-mechanical coupling of groundwater with multiple aquifers and aquitards. Subsidence is observed until the shutoff of access pit wells on February 19, 2015. This initiated a time period of opposing deformational processes, where coarse-grained deposits within the upper, unconfined aquifer began to elastically rebound while fine-grained deposits continued to compress as a result of time-dependent consolidation behavior (e.g., Chen et al., 2007; Gambolati and Teatini, 2015; Waltham, 2002) in combination with compaction of the confined aquifer, as deep well pumping rates remained constant during this time. After the remaining wells were shut off, instantaneous and spatially heterogeneous uplift was observed at rates as high as 17 cm/yr. Rebound rates were observed to exceed those of initial subsidence, likely because most wells were shut off over a two-day period in January 2016 after being sequentially turned on over several weeks between October and November 2014, allowing for a more rapid recovery of groundwater table elevation.

The mapped surface rebound shows that areas of greatest rebound are not found in areas of greatest initial subsidence, and that most subsided areas experienced some degree of permanent deformation. This is especially apparent at point PA, which lies in a region that initially subsided more than 3 cm, but experienced little to no rebound. As it is well-known that clay-rich deposits can be orders of magnitude more compressible than sand when drained [43,72,73], the majority of permanent deformation can be attributed to the compaction of low-permeability aquitard layers. The magnitude of permanent deformation, therefore, depends on the depth and thickness of these clay-rich deposits, which are known to vary greatly within the subsurface [58–60], resulting in spatially variable ground rebound (Figure 3.5). This non-uniform surface rebound created differential deformation of magnitudes greater than 2 cm across distances shorter than 100 m in some locations for a period of time, enough to pose a hazard to overlying infrastructure [74–76].

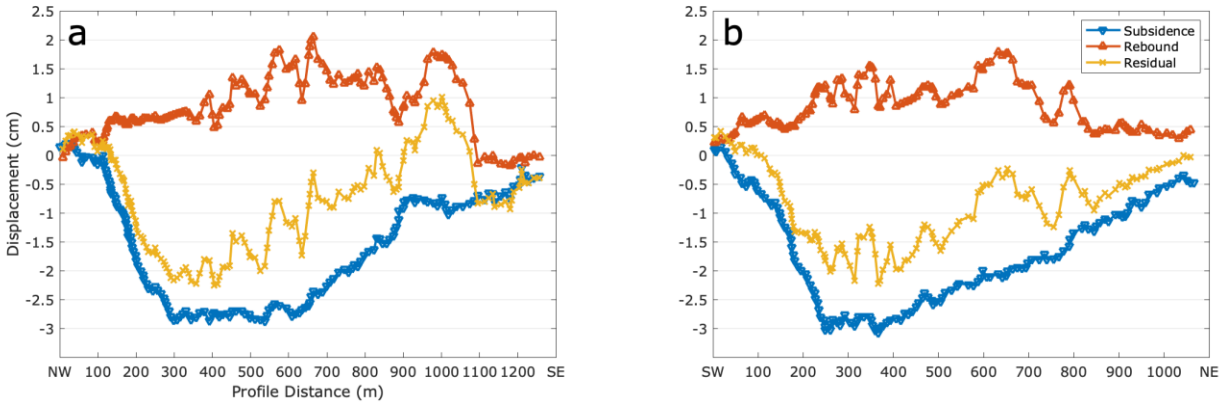

Figure 3.5 Subsidence, rebound, and residual subsidence from a) NW-SE and b) SW-NE profiles are shown in Figure 3.2c. Subsidence shown from Samsonov et al. RADARSAT-2 data spans August 31, 2014 to August 26, 2015, rebound data from Sentinel-1 spans January 12, 2016 to August 5, 2016.

A five-month lag is observed between the start of deep well pumping and the onset of subsidence at point PV, located at the steam plant where groundwater table elevations were lowered by 7.5 m in the months after deep well pumping began (Figure 3.4b). Delayed subsidence rates in areas outside of the initial subsidence event, including the steam plant, are less than 1 cm/yr, but continue in some locations until July 2019, over three years after the final wells were shut off. This widespread lagging subsidence is likely caused by time-dependent consolidation of fine-grained deposits within the confined aquifer, the full extent, depth, and thickness of which are poorly constrained. Point PZ subsides over 2 cm by October 2018 and is located 2.7 km away from the access shaft and dewatering wells, suggesting that delayed subsidence likely extends beyond the area shown in Figure 3.2d. A small degree of rebound is observed at points PV-PZ, likely due to an elastic response within coarse-grained layers. Some areas, including points PQ-PT, are observed to fully rebound. This indicates sediments in

these locations are primarily composed of coarse-grained material, allowing for a full elastic recovery in response to the restored pore water pressure.

3.7 Conclusions

Data show that hydro-mechanically coupled rebound can be highly unpredictable and poses a hazard to overlying infrastructure in urban environments underlain by highly variable geology, suggesting that more cautious approaches should be used when decommissioning dewatering wells in such areas. Delayed subsidence extended over 3 km away from all wells and lasted for over three years after they were shut off, indicating that the deepest wells had accessed groundwater from the upper reaches of the confined Puget Sound aquifer. Areas impacted by delayed subsidence display a full continuum of elastic behavior, where areas composed of coarser-grained sediments make a full elastic rebound, while areas composed of finer-grained deposits undergo extended subsidence and less rebound. The spatial variability of rebound and duration of post-dewatering surface deformation are well-captured by high-resolution SAR data that can monitor spatially- and temporally-dynamic groundwater interactions with subsurface strata in greater detail than other point-based monitoring systems.

3.8 Acknowledgments

This work was supported by the University Transportation Center for Underground Transportation Infrastructure (UTC-UTI) at the Colorado School of Mines for funding this research under Grant No. 69A3551747118 from the U.S. Department of Transportation (DOT). The opinions expressed in this paper are those of the authors and not the DOT. The authors would like to thank the European Space Agency for providing Sentinel mission data. Special thanks to Gabriel Walton for contributing MatLab codes and manuscript edits.

CHAPTER 4 - MAPPING URBAN EXCAVATION INDUCED DEFORMATION IN 3D VIA MULTIPLATFORM INSAR TIME-SERIES

4.1 Abstract

Excavation of a subway station and rail crossover cavern in downtown Los Angeles, California, USA induced over 1.8 cm of surface settlement between June 2018 and February 2019 as measured by a ground-based monitoring system. Point measurements above the excavation were extracted from Interferometric Synthetic Aperture Radar (InSAR) time-series analyses using multiple sensors with different wavelengths. These sensors include C-band Sentinel-1, X-band COSMO-SkyMed, and L-band Uninhabited Aerial Vehicle SAR (UAVSAR). The InSAR time-series point measurements were interpolated to continuous distribution surfaces, weighted by distance, and entered into the Minimum-Acceleration (MinA) algorithm to calculate 3D displacement values. This dataset, composed of satellite and airborne SAR data from X, C, and L band sensors, revealed previously unidentified deformation surrounding the 2nd Street and Broadway Subway Station and the adjacent rail crossover cavern, with maximum vertical and horizontal deformations reaching 2.5 cm and 1.7 cm, respectively. The analysis shows that airborne SAR data with alternative viewing geometries to traditional polar-orbiting SAR satellites can be used to constrain horizontal displacements in the North-South direction while maintaining agreement with ground-based data.

4.2 Introduction

The increasingly extensive archives of SAR data collected by various sensors on spaceborne and airborne platforms offer a variety of wavelengths and distinct viewing geometries from which surface deformation measurements can be made. Over the past 20 years, advances in time-series processing methods, including the Small Baseline (SBAS) subset technique and Persistent Scatterer Interferometry (PSI), have provided the ability to make deformation measurements with millimeter-scale accuracy and precision [10–13,77,78]. As datasets from more sensors at greater spatial and temporal resolutions become available, the question arises of how to combine complementary pieces of information within different SAR datasets effectively. The combination of displacement data from multiple SAR platforms, i.e., from different line of sight (LOS) vectors, can improve our ability to resolve the East, North, and Up components of the observed surface displacements [18]. This combination is necessary for comparison to ground based datasets and overcomes one of the main limitations of InSAR, in which a dataset from one track can measure displacements only in a single LOS projection.

Previous literature has shown agreement between multiple SAR datasets [79–88], proven the ability to integrate satellite and ground-based geodetic data [89–111], and offered some technical solutions for combining satellite-InSAR-based measurements into vertical, 2D, or 3D displacements [112–121]. Early successes in extracting 2D displacements were carried out by combining both left and right looking acquisitions from ascending and descending orbits [112]. Other techniques have used pixel offset

tracking to overcome low N-S deformation sensitivity, however these methods require deformations on the order of 10 cm or more and therefore are most often applied to large and temporally discrete deformation phenomena such as co-seismic or volcanic deformation [113,114]. More recent advances include the multidimensional small baseline (MSBAS) subset technique [6,15] and the Minimum-Acceleration (MinA) algorithm [16,17], both of which operate by combining multiple InSAR time-series datasets and solving a set of underdetermined linear equations via Tikhonov regularization or singular value decomposition. By combining ascending and descending tracks from multiple InSAR datasets, these algorithms allow for both 3D displacement extraction and increase the temporal resolution of displacement measurements.

The primary obstacles to extracting 3D displacements using only InSAR data are twofold. First, most InSAR sensors are side-looking systems onboard satellites traveling along polar orbit paths in a primarily N-S direction, preventing LOS measurements outside of a primarily E-W plane and therefore obscuring horizontal deformation in the N-S direction [67]. Second, combining multiple InSAR time-series can require an overlap between Persistent Scatterer (PS) pixel locations across multiple datasets. This combination can be especially tricky considering the variety of wavelengths and spatial resolutions from available sensors, each with inherent advantages and disadvantages, depending on the setting in which they are applied [19,52,53,122]. Acquiring sufficient density of PS pixels between separate InSAR datasets can be a challenge, especially when applying time-series techniques in natural environments with low amplitude backscatter [13,123].

Here we present a method to overcome each obstacle by 1) using Uninhabited Aerial Vehicle SAR (UAVSAR) data [89,124–132] with primarily N-S LOS orientations, in combination with Sentinel-1 and COSMO-SkyMed data, to better constrain displacements in the N-S direction and 2) inverse distance weighting each path of InSAR datasets, based on PS pixel location, in order to use all available data. The weighted datasets are then entered into the MinA algorithm to calculate 3D displacement values [16–18]. This method is tested on a spatially acute (30000 m^2) subsidence event in downtown Los Angeles, California, and compared to available ground-based observations to quantitatively assess method accuracy and precision. In this framework, combined InSAR datasets can monitor 3D deformations of highly urbanized zones with great spatial and temporal resolution.

4.3 Background

The Regional Connector Transit Corridor (RCTC) project consists of a 3 km-tunnel connecting the blue and gold metro rail lines in downtown Los Angeles, California, USA (Figure 4.1). The construction includes a shallow (~15 m top depth) 90 m long, 17.7 m wide, 11 m tall crossover structure that began construction after twin 6.7 m diameter tunnels were bored by an earth pressure balance tunnel-boring machine. Boreholes along 2nd Street contain a top layer of artificial fill ranging from 1-3 m thick that overlies a 2-7 m thick deposit of poorly sorted alluvial sand. A perched aquifer is found within the

alluvial sands 3-4 m below street level between Hill Street and Main Street. The regional groundwater table begins near the interface between the alluvial sands and the underlying weathered siltstone bedrock of the Fernando formation [133].

Adjacent to the crossover cavern is the 2nd and Broadway station, for which excavation was completed in July 2018 using the cut and cover method. Sequential excavation of the crossover cavern took place from May 30, 2018 to March 14, 2019, after which 30 and 46 cm liners of shotcrete and concrete, respectively, were installed. Sequential excavation follows principles of the observational method, requiring a detailed monitoring system with extensive instrumentation, including a network of Ground Surface Settlement Points (GSSP) and automated total stations. This monitoring system captured an increase in surface subsidence coincident with the crossover cavern excavation. Between June 2018 and February 2019, a maximum vertical settlement magnitude of 1.8 cm was measured along 2nd Street directly above the cavern by GSSP, with peak deformation rates exceeding 2.5 cm/yr [134].

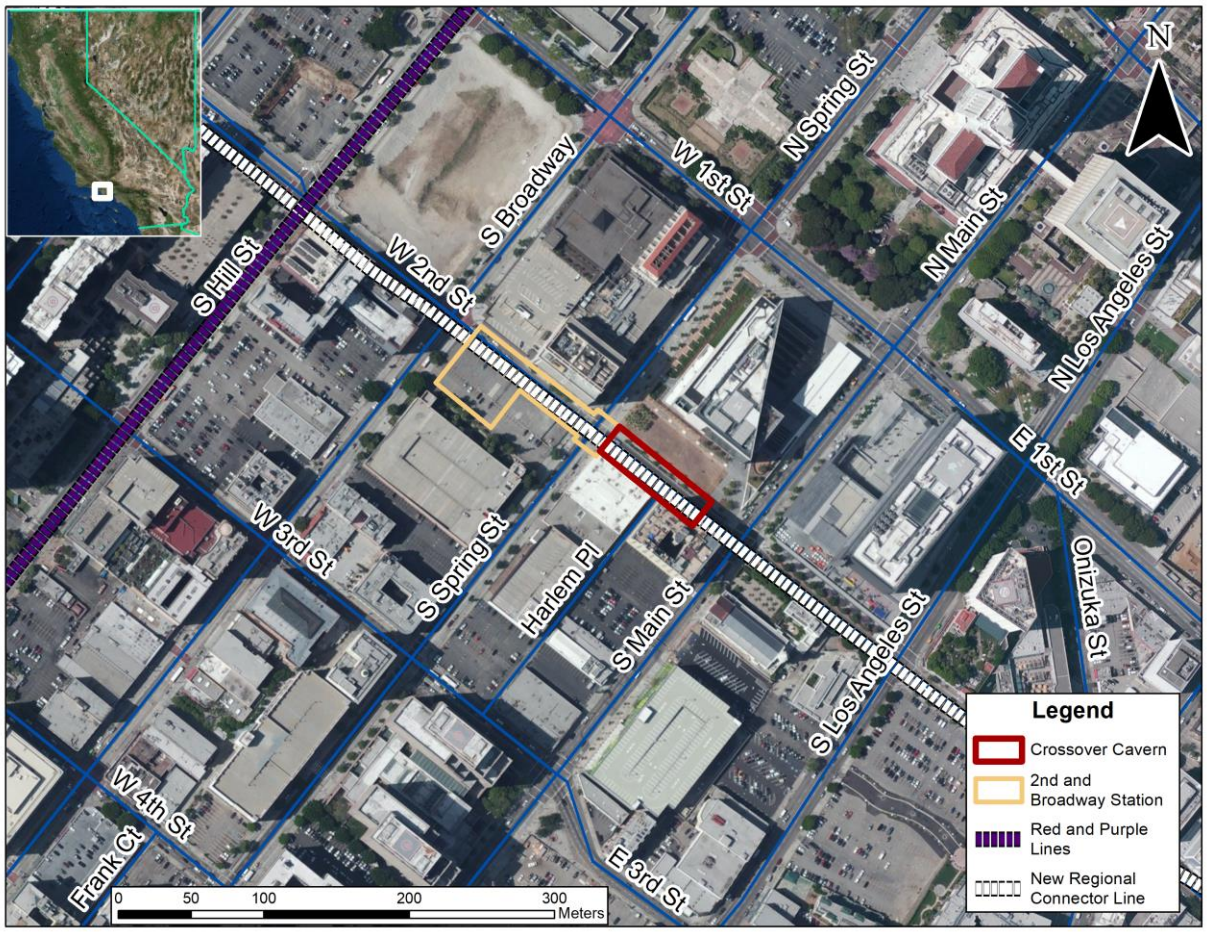

Figure 4.1 Location of Los Angeles subway extension, including 2nd and Broadway station and adjacent crossover cavern

The spatial extent and magnitude of ground deformation caused by tunneling activities are primarily influenced by the size and depth of excavation, geology, and

hydrologic setting. Tunneling projects in urban environments generally yield relatively low magnitude settlements, as extra precautions are taken to avoid damaging overlying infrastructure. To more fully explore this deformation event, we have synergistically combined SAR data from three sensors: Sentinel-1, UAVSAR, and COSMO-SkyMed. Each sensor and path provided a distinct viewing geometry (Table 4.1). LOS deformation time-series of all data paths were entered into a modified version of the MinA multiplatform InSAR algorithm to overcome the unique challenges presented by urban settings and yield accurate 3D displacement information. The InSAR-derived 3D displacements were compared to the GSSP dataset to assess the data accuracy and test the applicability of the MinA algorithm on small magnitude urban subsidence events.

Table 4.1 InSAR dataset information

Sensor	Path	LOS Azimuth	Incidence Angle	Spatial Resolution (m)	Time Span	Number of Acquisitions	Maximum Baseline (m)
Sentinel-1	137	77°	44°	2.3x14.1	Jan 9, 2018 - Jul 3, 2019	66	163
Sentinel-1	71	283°	39°	2.3x14.1	Jan 10, 2018 - Jun 22, 2019	45	126
Sentinel-1	64	77°	34°	2.3x14.1	Jan 4, 2018 - Jun 28, 2019	40	116
COSMO-SkyMed	-	279°	53°	1.7x2.0	Jan 12, 2018 - Jul 5, 2019	25	758
UAVSAR	08523	356°	55°	1.7x0.6	Apr 23, 2009 - Feb 21, 2019	15	N/A
UAVSAR	26524	174°	52°	1.7x0.6	Apr 23, 2009 - Feb 21, 2019	18	N/A

4.4 Data and Methods

Measurements of ground deformation associated with excavations for the RCTC project were acquired by processing Single Look Complexes (SLCs) from 3 paths of Sentinel-1, 2 paths of UAVSAR, and a single descending path of COSMO-SkyMed data (Table 4.1). Each path was separately processed using repeat pass differential interferometry. GAMMA software [135] was used to create a series of single master interferograms from all data paths. A single master date was chosen for each data path, and slave images were co-registered to the geometry of the chosen master scenes. Topographic

phase contribution was removed via the USGS 3D Elevation Program (3DEP) 1 m resolution Digital Elevation Model (DEM, http://nationalmap.gov).

GAMMA's Interferometric Point Target Analysis (IPTA) was used to create a time-series of Persistent Scatterers (PS). PS pixels were identified using the Mean to Standard-deviation Ratio (MSR) of the radar intensity backscatter. A threshold MSR value of 1.1 was used to select pixels with low temporal variability, high-intensity backscatter that provided stable phase returns over the time period of interest. SLC values at PS pixel locations were extracted and written to a point data stack. Initial differential interferograms were formed and analyzed in the temporal domain to measure the linear dependence between the perpendicular baseline and phase for each PS pixel, which was used to calculate and correct DEM error. These corrections were subsequently used to update calculated perpendicular baseline values. Linear deformation rates were then calculated for each pixel. Residual phase change, considered as a deviation from the linear deformation rate, is composed of atmospheric contamination, baseline measurement errors, any non-linear deformation, and random noise. As the atmospheric phase contribution from the master scene correlates in space and time, it was extracted using a low-pass temporal filter of the residual phase, then removed from all interferograms. The process was then iterated using the corrected DEM, updated perpendicular baselines, and atmosphere-corrected interferograms. Final deformation values were produced via a phase unwrapping algorithm based on minimum cost flow techniques applied to a Delaunay triangular network.

After the LOS deformation time series of PS pixels were constructed for all input datasets, each dataset was then individually interpolated to a common 1m gridded surface and combined in a post-processing stage using the MinA algorithm to calculate 3D deformation. As the MSBAS technique requires simultaneous processing and unwrapping of many interferograms, we have chosen to apply the MinA algorithm due to its ability to ingest PSI time-series data and its simple post-processing application. LOS displacement rates were calculated for all input data at each acquisition time across all datasets. Because spatial resolution and LOS differed for each input dataset, PS pixel locations and scatterers also varied (Figure 4.2). This variability prevented any one sensor from viewing the entirety of the deforming area, and required that each dataset be weighted by inverse distance from the nearest PS pixel. This is the primary change from the original MinA algorithm, which used pixel coherence as the primary weighting factor. Weighted LOS displacement rates were then connected to the unknown 3-D velocities, creating a system of underdetermined independent linear equations:

$$\begin{bmatrix} d_E \\ d_N \\ d_U \end{bmatrix} = \begin{bmatrix} \Gamma d_{LOS^{(1)}} \sin\vartheta^{(1)} \cos\varphi^{(1)} & \Gamma d_{LOS^{(1)}} \sin\vartheta^{(1)} \sin\varphi^{(1)} & -\Gamma d_{LOS^{(1)}} \cos\vartheta^{(1)} \\ \Gamma d_{LOS^{(2)}} \sin\vartheta^{(2)} \cos\varphi^{(2)} & \Gamma d_{LOS^{(2)}} \sin\vartheta^{(2)} \sin\varphi^{(2)} & -\Gamma d_{LOS^{(2)}} \cos\vartheta^{(2)} \\ \vdots & \vdots & \vdots \\ \Gamma d_{LOS^{(n)}} \sin\vartheta^{(n)} \cos\varphi^{(n)} & \Gamma d_{LOS^{(n)}} \sin\vartheta^{(n)} \sin\varphi^{(n)} & -\Gamma d_{LOS^{(n)}} \cos\vartheta^{(n)} \end{bmatrix} \quad (2)$$

where Γ is the weighting factor determined by the inverse distance to the nearest PS pixel, ϑ and φ are the radar incidence angle and LOS azimuth, respectively, of the n LOS displacement time series. Equations were solved in the least squares sense by using first-order Tikhonov regularization [136]. Regularization was achieved by imposing

constraints to minimize the acceleration of 3D displacements between acquisitions. These constraints were imposed using the L-curve method [137,138] whereby a range of regularization coefficients are applied to the input system of linear equations. This creates a series of potential solutions, ranging from solutions that fit the data perfectly without minimizing acceleration to solutions that minimize acceleration but do not necessarily fit the input data. All potential solutions plot along an L shaped curve, with the optimum solution located at the bottom left corner. The solution found at the corner of the L-curve is optimized because it provides the most precisely balanced solution between minimizing solution error and minimizing displacement acceleration. This analysis was performed using the regularization tools Matlab package [139]. Once estimated, the calculated velocities were independently time-integrated to extract a single 3D deformation time series.

All available UAVSAR acquisitions were used in order to produce a deformation time-series, but only four acquisitions were made during the time period of interest, on November 16, 2018 and February 21, 2019 for both UAVSAR data paths. Due to the poor temporal resolution of the UAVSAR data, they are only available to constrain N-S horizontal deformation during the time between these acquisitions. Before November 16, 2018 and after February 21, 2019, N-S acceleration values were assumed to be negligible in order to account for the low sensitivity of satellite InSAR measurements in this direction [29]. To assess the accuracy and precision of the applied method, calculated vertical deformations from InSAR data were compared to and differenced with those from a network of GSSP that captured the subsidence event in real-time.

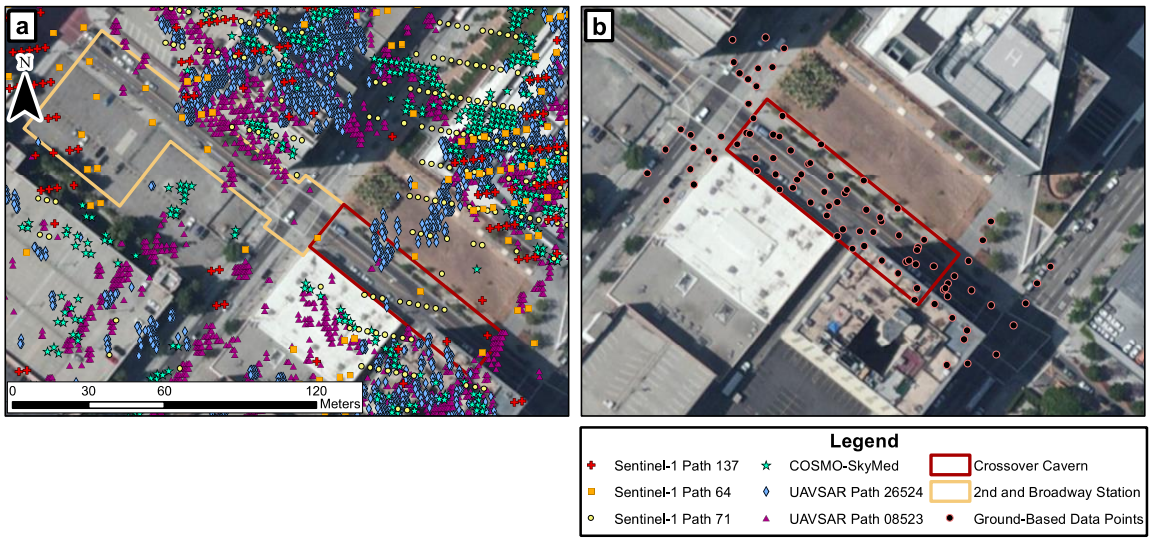

Figure 4.2 a) Persistent scatterer pixel locations from spaceborne and airborne InSAR datasets. b) Ground Surface Settlement Point locations

4.5 Results

Calculated 3D deformations from all InSAR datasets reveal the temporal and spatial extents of subsidence related to excavation activities (Figure 4.3). Horizontal and vertical deformations were observed to reach beyond the boundaries of both the crossover cavern and the ground-based dataset, encompassing an area of approximately 200 m by 150 m. From November 16, 2018 to February 21, 2019, the period of time during which UAVSAR data are available to constrain N-S deformation (Figure 4.4), a maximum vertical deformation of 1.2 cm was measured directly above the crossover cavern near point PD. As this location is near the center of the subsiding area, observed deformation is primarily vertical and very little E-W or N-S horizontal deformation is calculated. Maximum horizontal deformations reach 0.5 cm at points PF, PC, PB, and PE for the North, South, East, and West deformation components, respectively. Calculated horizontal movements are consistent with a subsidence event, where horizontal deformations are directed toward the maximum settlement location. Localized pockets of subsidence appear near points PB, PC, and PE and coincide with spatially variable horizontal deformation. Computed N-S deformation contains a greater degree of spatial variability than E-W deformation. All deformation components contain greater amounts of noise and spatial heterogeneity on buildings.

Comparison between vertical InSAR and GSSP data shows the datasets are in good agreement, with a maximum absolute difference of 1.15 cm at point P1 and a maximum average difference of 0.53 cm at point P8 (Figures 4.5 and 4.6). Spatially, InSAR data tend to underestimate settlement in areas directly overlying the central portion of the crossover cavern, while slightly overestimating settlement northwest and southeast of the cavern. Points P1 and P2 undergo a period of slight uplift in Fall 2018, which is captured in both the InSAR and GSSP data, but overestimated by InSAR by several mm. Around the same time period, subsidence rates at points P3-P7 are observed to decrease in the GSSP data, a trend that is well captured by InSAR as well. Subsidence rates near the center of the crossover cavern remain constant in the GSSP data, but InSAR calculated subsidence rates decrease or even show periods of uplift (Figure 4.6h). This is the primary discrepancy between the InSAR and GSSP datasets, further illustrated by consistent underestimation of subsidence at points surrounding point P8 (Figure 4.5). Points P9-P12 show lower magnitudes of surface deformation, but generally show good agreement between InSAR and GSSP data.

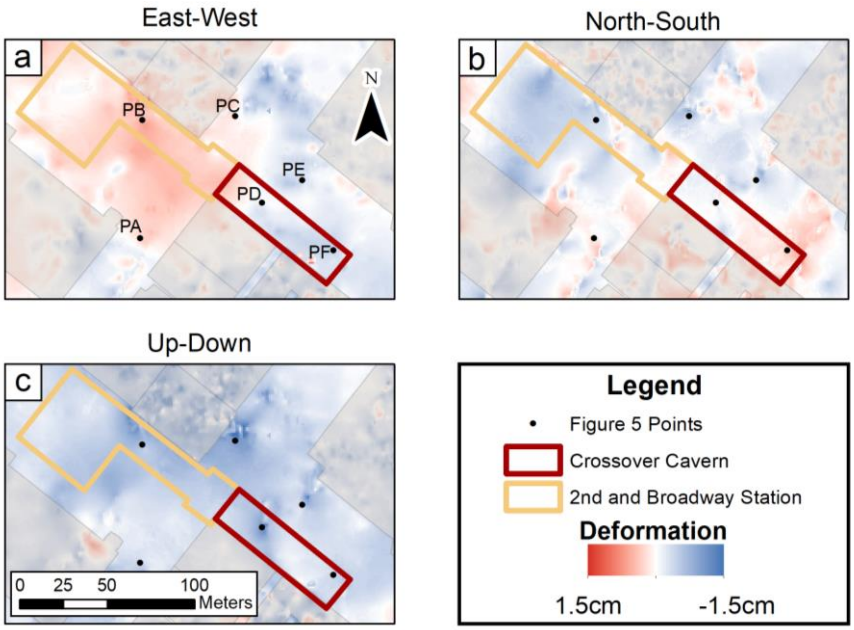

Figure 4.3 Map of surface deformation calculated from InSAR data spanning November 16, 2018 to February 21, 2019 in a) East-West, b) North-South, and c) Up-Down directions

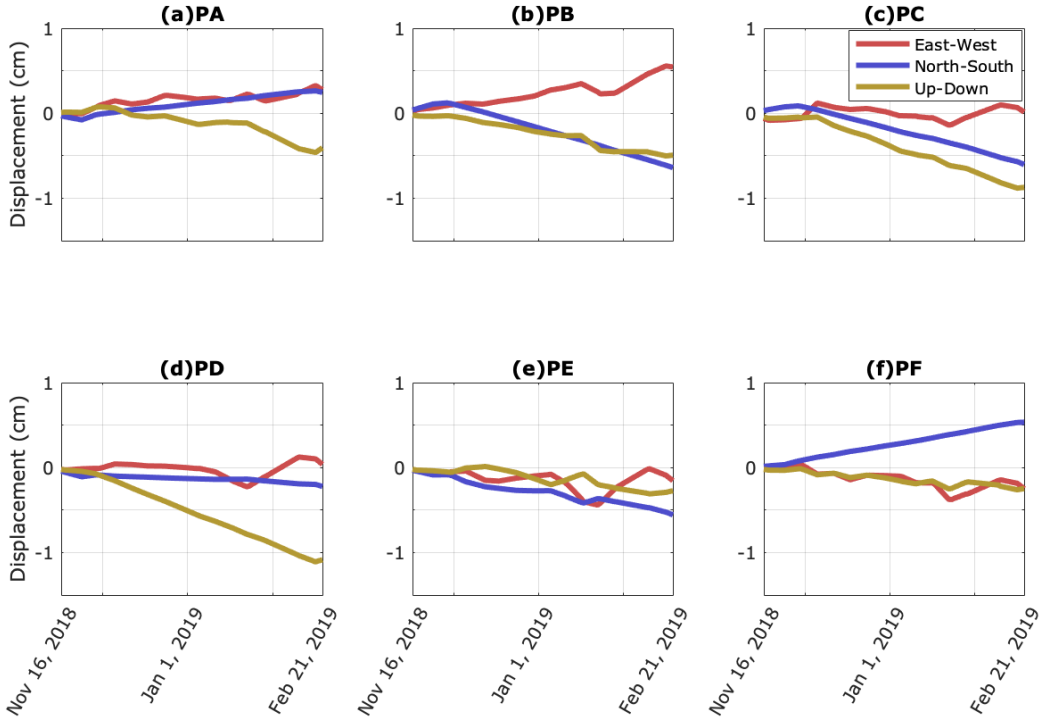

Figure 4.4 East-West, North-South, and Up-Down deformation components of point locations indicated in Figure 4.3

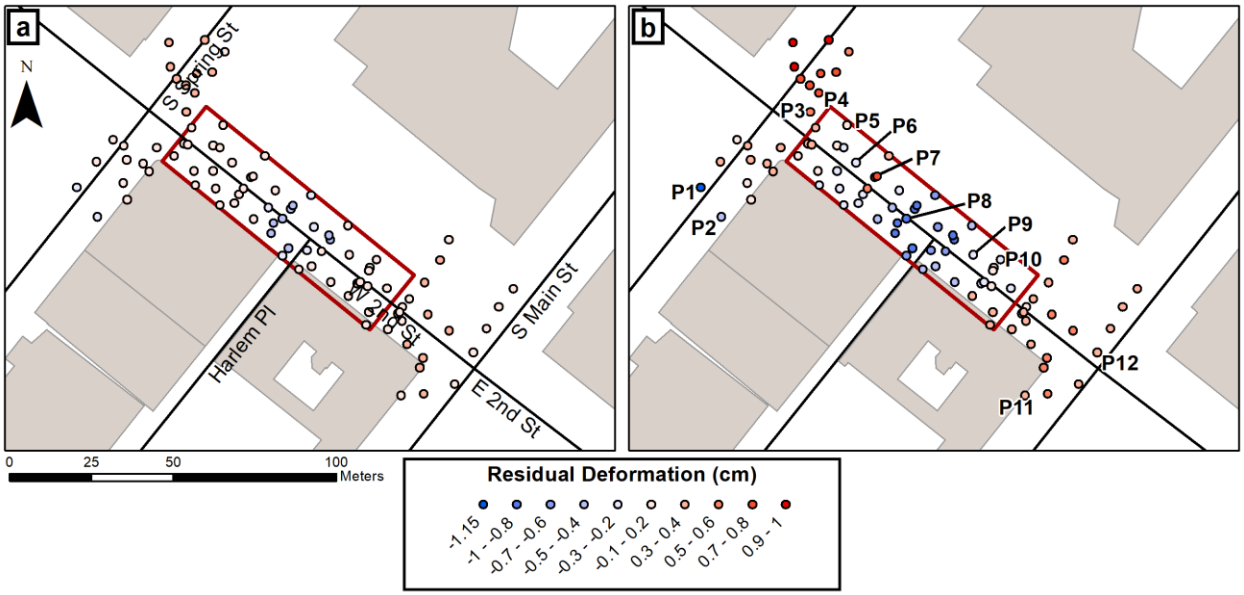

Figure 4.5 (a) Mean residual deformation (b) maximum residual deformation after differencing ground-based and InSAR vertical deformation data. Negative residuals indicate underestimation, while positive residuals indicate an overestimation of settlement by InSAR. Deformation time series for points P1-P12 shown in Figure 4.6

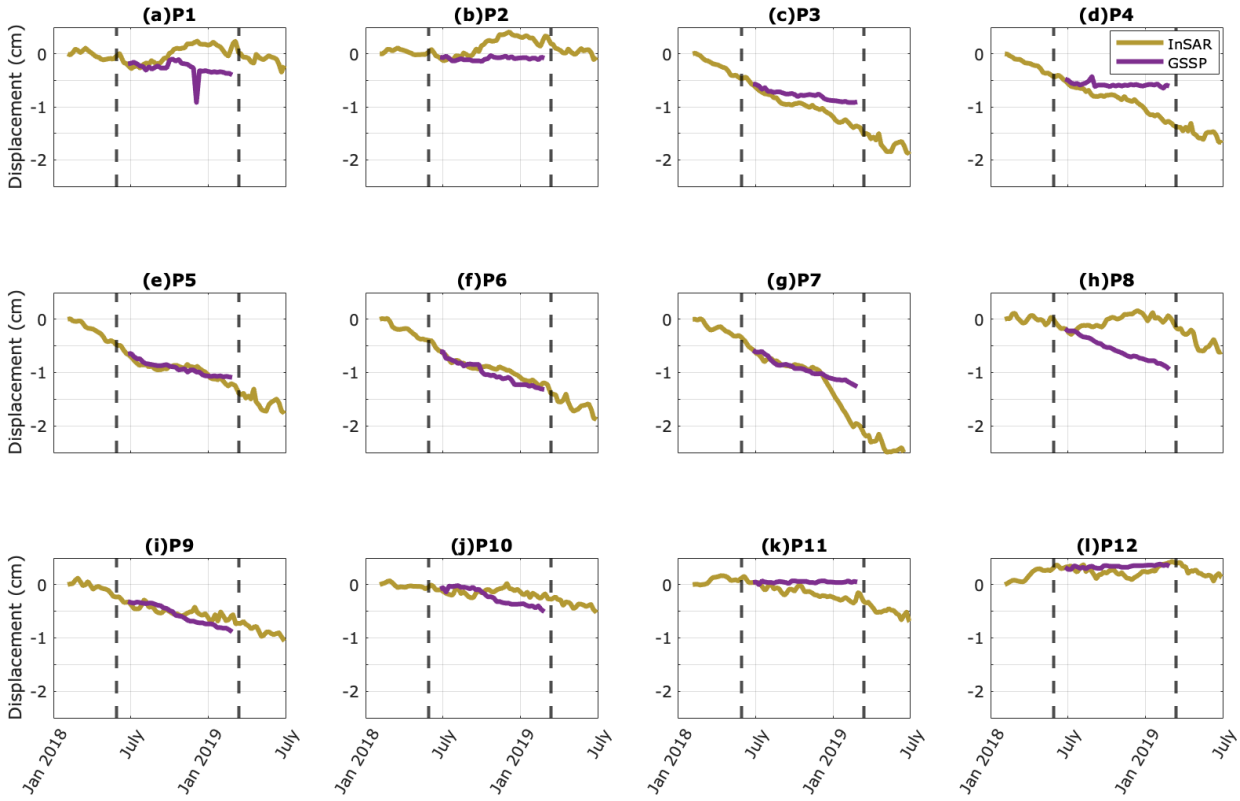

Figure 4.6 Comparison of vertical InSAR deformation and ground-based data from points indicated in Figure 5b. InSAR measurements span February 3, 2018 to June 28, 2019. Ground-based data acquired between June 25, 2018 and February 25, 2019. Vertical dashed lines represent the initiation and completion of the crossover cavern sequential excavation on May 30, 2018 and March 14, 2019

InSAR data reveal vertical deformation on the northwestern side of the cavern, near points P3 and P4, began as early as January 2018 and maintained an average subsidence rate of 1.3 cm/yr until the completion of the crossover cavern. This early period of subsidence is not present throughout the entirety of the study area. Early subsidence reaches as far to the east as point P9, but is not observed in points P10-P12. Average vertical deformation rates during the time period of measurement are greatest at point P7, with rates reaching 1.6 cm/yr. The maximum average settlement rate measured by GSSP data at point P8 is 1.3 cm/yr. After sequential excavation of the crossover cavern was completed in March 2019, InSAR derived deformation show continued subsidence until the end of the time series in July 2019. This post-excavation subsidence occurs at lower rates near points that undergo very little pre-excavation deformation, and is slightly faster at points that undergo greater pre-excavation deformation.

4.6 Discussion

Urban excavation processes induce ground deformation through the collapse of soils into underground voids or by the extraction of groundwater in unconsolidated deposits. This deformation can cause damage to roads, buildings, and utility lines. It is therefore critical to control the ground deformation within certain limits, especially in urban environments with overlying infrastructure. InSAR exploits the phase shift between SAR acquisitions and is a powerful technique for measuring ground settlement over time. However, the urban environment poses unique challenges to single sensor and single platform InSAR analysis. Multiplatform InSAR time-series provide an opportunity to overcome the obstacles presented by urban noise and spatially narrow study areas.

InSAR time-series analysis reveals the timing and magnitude of subsidence associated with the excavation of portions of the RCTC subway extension in downtown Los Angeles. While ground-based data were focused on deformation related to the sequential excavation of the crossover cavern, InSAR data reveal vertical deformation on the western side of the cavern began in early 2018, months before sequential excavation of the cavern initiated (Figure 4.6c-g). This is likely due in part to the boring of the twin tunnels and cut and cover excavation at the 2nd and Broadway station, which began construction in early 2016 and finished excavation in July 2018 [16]. This is further supported by the presence of vertical and horizontal surface deformation located directly above the station (Figure 4.3 and Figure 4.4b). Similar deformation patterns are observed from the start of cavern excavation (Figure 4.7) and extend past its completion (Figure 4.8). The settlement would also be triggered by any dewatering that occurred within the shallow perched aquifer or deeper regional aquifer, in which case the extent and magnitude of subsidence are primarily controlled by geology and aquifer storage geometry [6,52,53]. Time dependent soil consolidation [43] due to dewatering or other groundwater regime disturbance could explain the continued subsidence after the completion of the crossover cavern excavation. The duration of continued subsidence would depend on the amount of clay within the drained sediments [45,46,48,81,140,141], as clays are more compressible and posses a lower hydraulic conductivity than larger grain sizes [72]. There would also be potential for hydro-mechanically coupled ground rebound post groundwater table recovery [69].

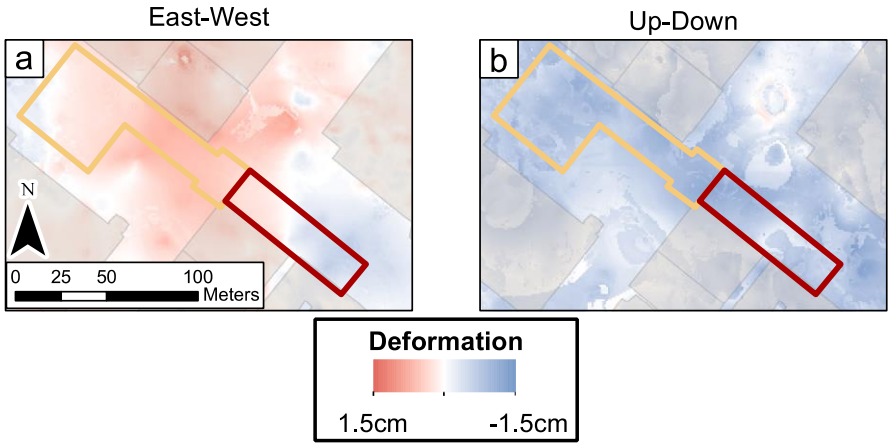

Figure 4.7 Vertical and East-West horizontal deformation spanning initial crossover cavern excavation from June 5, 2018 to November 11, 2018. Displacement measured by combined Sentinel-1 and COSMO-SkyMed time-series

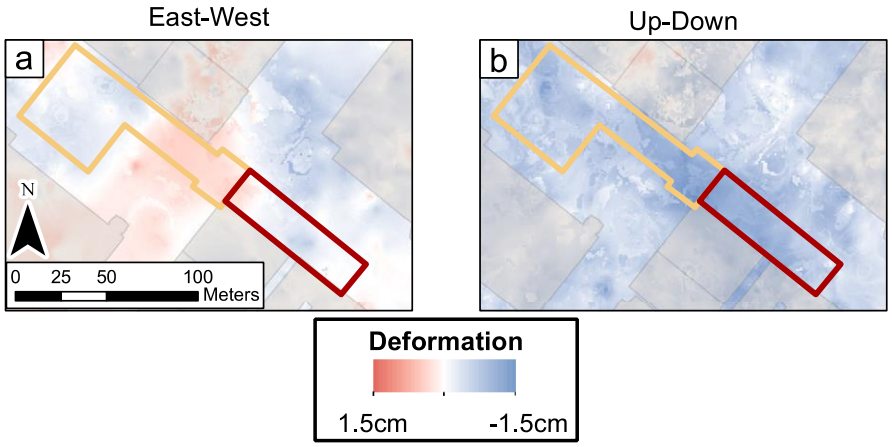

Figure 4.8 Vertical and East-West horizontal deformation spanning the final portion of crossover cavern excavation from February 27, 2019 to July 3, 2019. Displacement measured by combined Sentinel-1 and COSMO-SkyMed time-series

While the subsidence signal was clearly captured by InSAR, measurement accuracy was not consistent with the ground-based data at all locations. The single largest measurement difference occurred at point P1 due to an apparent outlier measurement of the ground-based data in December 2018. Point P8 possesses the most consistent discrepancies between the InSAR and GSSP datasets (Figure 4.6h). We attribute these discrepancies to limited PS pixel coverage, as Sentinel-1 provided the only PS pixels

near the center of the crossover cavern (Figure 4.2a). Since these data possess the lowest spatial resolution of all input datasets (Table 4.1), measurements near this portion of the cavern rely on only a handful of PS pixels. These PS pixels appear not to capture the full magnitude of subsidence, as average and maximum residuals show a consistent underestimation of settlement near the intersection of Harlem Place and 2nd Street (Figure 4.5). InSAR calculations slightly overestimate uplift observed at points P1 and P2 in Fall 2018. The fact that uplift is observed in both the InSAR and GSSP datasets, along with a decrease in subsidence rate at points P3-P7 around the same time, indicate that the signal is not simply noise. One potential source of the decreased subsidence rates could be the installation of ground support during the sequential excavation. Such supports are exposed to the least amount of stress directly after installation near the face of the excavation but are subject to deformation as stress increases while excavation continues. Though the tunnel supports undergo deformation themselves, surface deformation would take place at a lower rate than it would for an unsupported excavation.

UAVSAR data produced more PS pixels along the crossover cavern, especially on the westbound side of 2nd Street toward Spring Street (Figure 4.2a). InSAR and GSSP data are in good agreement in this area, aside from point P7, which possesses the largest overestimation of settlement by the InSAR data (Figure 4.5b). The increase in InSAR measured subsidence at P7 takes place during the time period in which UAVSAR data are available (November 16, 2018 to February 21, 2019). We attribute this overestimation in part to the relatively poor temporal resolution of the UAVSAR datasets, as only four scenes are available during the period of interest. Such coarse temporal resolution increases the difficulty of accurately calculating and removing atmospheric and other noise sources, and makes transient surface changes more difficult to identify. This difficulty is visually apparent in the North-South displacements (Figure 4.3b), which are primarily controlled by the UAVSAR datasets. The calculated North-South displacements resemble that of a subsidence signal, where horizontal motion is directed toward a plane centered at the point of maximum subsidence, but the N-S horizontal deformation is spatially inconsistent relative to the smoother E-W horizontal displacements (Figure 4.3a) that are better captured by satellite data with higher temporal resolution. Additionally, L-band wavelength sensors, while able to maintain coherence over longer timespans than C-band or X-band sensors, are known to possess less accurate LOS deformation measurements compared to shorter wavelength sensors [142]. Other sources of artifact inducing noise may include thermal expansion and contraction of buildings [133], surface changes due to ongoing construction related to the cut and cover of the 2nd and Broadway station, interpolation error within the LOS time-series input, other urban noise [122,135], or discrepancies related to wavelength-dependent scattering phenomena [53]. The impact of artifacts within the dataset could be partially mitigated by applying a 4D filter that can remove random noise from low magnitude subsidence events [52]. Timing of the initiation of subsidence can be constrained by analysis of archival SAR data.

The InSAR PS post-processing algorithm shown here is specifically designed for application to deformation events in which the majority of displacement occurs in a

single direction, which is subsidence for the case study shown here. As the MinA algorithm succeeds in calculating 3D displacement data by assuming minimum acceleration in all directions, it is not well suited for application to dynamic deformation events, such as landslides, where large magnitudes of vertical and horizontal displacements can occur simultaneously [54,55,143]. Interpolation of each dataset also presents potential sources of error in cases of spatially heterogeneous deformations that are not accurately captured by available PS pixels. A high PS pixel density across InSAR datasets is also required to carry out distance weighting with sufficient LOS viewing constraints. Here we assume that all sensor wavelengths are equally accurate and precise in their ability to capture deformation magnitudes at their PS pixel locations, though this may not be true in all situations and more research is required to better quantify measurement uncertainty when combining multiple InSAR datasets of different wavelengths.

4.7 Conclusions

Combined satellite and airborne SAR data from X, C, and L band sensors reveal 3D deformation surrounding the 2nd and Broadway subway station and the adjacent rail crossover cavern in downtown Los Angeles, encompassing an area of 30000 m^2 with maximum vertical and horizontal deformations reaching 2.5 cm and 1.7 cm, respectively. Vertical displacements calculated by combining six paths of InSAR data were in good agreement with available ground-based data, within 5 mm on average. InSAR calculation accuracy was observed to decrease in areas with less PS pixel coverage. UAVSAR data provided necessary constraint of N-S horizontal deformation, but were limited by low temporal resolution. Both interpolating and distance weighting InSAR datasets overcame challenges presented by limited overlapping PS pixel coverage.

These results support the application of the distance weighted MinA algorithm to small magnitude, spatially acute subsidence events given input data with sufficiently dense PS pixel spacing relative to the size and shape of ground deformation and diverse LOS viewing geometries. As more SAR platforms become available, including the recent launch of the SAOCOM SAR constellation and future launch of NASA-ISRO SAR mission, post-processing algorithms like the MinA algorithm can be used in combination with multiple SAR datasets to compare to or potentially replace ground based geodetic systems for monitoring purposes.

4.8 Acknowledgments

This work was supported by the University Transportation Center for Underground Transportation Infrastructure (UTC-UTI) at the Colorado School of Mines under Grant No. 69A3551747118 from the U.S. Department of Transportation (DOT). Special thanks to the National Aeronautics and Space Administration Jet Propulsion Laboratory for providing UAVSAR data. Project carried out using CSK® Products, © ASI (Italian Space Agency), delivered under an ASI license to use.

CHAPTER 5 - GENERAL CONCLUSIONS

As subsurface excavation technologies continue to advance, tunneling has become increasingly common for both transportation and energy production applications. This necessitates the ability to monitor excavation-induced subsidence over large areas in a wide range of geologic and hydrologic settings, especially when ground-based measurements are unavailable. InSAR based surface displacement measurements are ideal for mapping the spatial extent of deformation events, though they are subject to multiple potential sources of noise depending on the environment in which the technique is applied. Natural terrains are notoriously difficult in regard to InSAR application because of the temporal decorrelation phenomenon, whereby vegetative growth or other natural surface changes over time introduce noise capable of preventing meaningful displacement measurements. Urban environments contain buildings and structures that provide more stable reflecting surfaces than vegetated environments, but are also subject to certain noise sources such as thermal expansion and contraction of buildings that can be difficult to quantify and remove. High-resolution InSAR data from a new generation of satellites offer the opportunity to post-process InSAR time-series data and reduce noise. The research within this report illustrates through three case studies how post-processing of large, temporally dense LOS InSAR time-series datasets can reduce interferometric noise to more accurately and precisely map and measure subsidence in both natural and urban environments.

5.1 Major Contributions

A novel 4-D filtering algorithm was adapted to remove phase noise from InSAR time-series data and was tested on a Sentinel-1 dataset acquired during a tunneling induced subsidence event in the highlands of Sri Lanka, a highly vegetated, atmospherically variable location. Filtered data allowed for more precise determination of the timing, magnitude, spatial extent, and duration of induced subsidence, and was used to clarity the relationship between tunneling activities and aquifer depletion. This algorithm can be applied to elucidate subsidence events by reducing atmospheric, vegetative, and random noise through simultaneous spatial and temporal filtering.

Multi-track Sentinel-1 data measured subsidence induced by dewatering during excavation of the Alaskan Way Viaduct replacement tunnel in Seattle, WA. Measurements were converted to vertical displacements using the MinA algorithm and validated through comparison to the alternative MSBAS algorithm. This analysis revealed the potential for a subsided urban landscape to undergo potentially hazardous differential rebound via post-dewatering restoration of pore pressure in spatially variable glacial sediments. Widespread delayed subsidence was also identified, likely due to compaction of sediment due to pumping from a deeper regional aquifer.

The MinA algorithm, with added distance weighting, was applied to subsidence induced by the excavation of a new subway line in downtown Los Angeles, CA. 3D displacements were calculated through optimization of multiple spaceborne and airborne InSAR datasets and validated via comparison to available ground-based data, revealing a wider extent of subsidence than was previously known. This work revealed

that N-S horizontal displacements can be calculated with higher accuracy and precision when combined with airborne InSAR datasets with favorable viewing geometries. This ability is crucial to allow InSAR data to be more easily compared to ground-based observations during tunnel construction.

Post-processing through either 4-D filtering or application of the MinA algorithm revealed the true extent of surface displacements that were previously unrecognized or not captured by ground-based data. Knowing the full extent, duration, and magnitude of excavation-induced subsidence can be crucial to mitigating their potential impacts. This research highlights the need for space based geodetic monitoring of tunneling projects, and offers practical solutions for its application. As more SAR platforms become available, including the recent launch of the SAOCOM SAR constellation and future launch of NASA-ISRO SAR mission, post-processing algorithms can be used to combine data from multiple SAR inputs to compare to or potentially replace ground based geodetic systems for monitoring purposes. Current satellite capabilities can provide near daily measurements, but temporal resolution may be further enhanced in the future by using constellations of small satellites with potential to make hourly observations. Current small SAR satellite constellations are being tested and will likely be available within the next 10 years. This will provide another significant enhancement and additional opportunities to monitor excavation induced surface displacements using space-based geodetic methods.

5.2 Recommendations for Future Research

InSAR has proven to be an effective tool for identifying and measuring excavation induced subsidence, and an abundance of both contemporary and historical data will allow space-based geodetic research of tunneling activities to continue well into the future. As of the writing of this report, InSAR detection of surface displacements in natural environments still poses a major challenge. The coherence based PS approach offered by StaMPS, first released in 2004, remains one of the most commonly used softwares for extracting PS in non-urban settings. Further advances in this area of study will be crucial to better identify settlement from rural tunneling projects. This lack of knowledge could be alleviated somewhat in the next few years after the launch of NASA-ISRO NISAR satellite, which will provide freely available L-band data. Longer wavelength data can better penetrate heavy vegetation, and is crucial for maintaining interferometric coherence in such environments. Temporal decorrelation can also be minimized by improving the temporal resolution of the data, indicating that future small SAR satellite constellations could provide data at a high enough rate to identify and minimize phase noise introduced by vegetation.

Though PS extraction is relatively simpler in urban environments, pixels are still subject to various sources of noise. Some of these noise sources, such as thermal expansion and contraction of buildings, have been identified previously but can be difficult to quantify and remove. Additional post-processing algorithms are therefore needed to address various urban noise sources. This may occur in combination with machine learning algorithms capable of automatically detecting specific features, e.g.

distinguishing between buildings and roads, and applying noise reduction filters to specific features. Such an approach could be used to automatically detect and remove thermal phase contributions from buildings, while avoiding unnecessary filtration of data within areas that do not contain buildings or structures. This adaptive system could be used to more precisely identify PS pixels, as current PS extraction approaches rely on the identification of a set of pixels that behave similarly over relatively large space and time scales. With sufficient spatial resolution, this approach could be used to identify discrepancies between the deformations of structures and surrounding areas, with potential to identify any associated structural damages.

Further research is also needed to compare internal tunnel deformation to measured surface deformation. This information can be used to assess current and forthcoming tunnel excavation support technologies that are designed to minimize surface settlements during construction. Though published InSAR surveys generally do not report a lack of deformation, applying the technique for evaluative purposes may encourage more extensive use of InSAR for underground construction applications in the future

REFERENCES

1. Tesauro, M.; Berardino, P.; Lanari, R.; Sansosti, E.; Fornaro, G.; Franceschetti, G. Urban subsidence inside the city of Napoli (Italy) observed by satellite radar interferometry. *Geophys. Res. Lett.* **2000**, *27*, 1961–1964, doi:10.1029/2000GL008481.

2. Strozzi, T.; Delaloye, R.; Poffet, D.; Hansmann, J.; Loew, S. Surface subsidence and uplift above a headrace tunnel in metamorphic basement rocks of the Swiss Alps as detected by satellite SAR interferometry. *Remote Sens. Environ.* **2011**, *115*, 1353–1360, doi:10.1016/j.rse.2011.02.001.

3. Strozzi, T.; Caduff, R.; Wegmüller, U.; Raetzo, H.; Hauser, M. Widespread surface subsidence measured with satellite SAR interferometry in the Swiss alpine range associated with the construction of the Gotthard Base Tunnel. *Remote Sens. Environ.* **2017**, *190*, 1–12, doi:10.1016/j.rse.2016.12.007.

4. Perissin, D.; Wang, Z.; Lin, H. Shanghai subway tunnels and highways monitoring through Cosmo-SkyMed Persistent Scatterers. *ISPRS J. Photogramm. Remote Sens.* **2012**, *73*, 58–67, doi:10.1016/j.isprsjprs.2012.07.002.

5. Barla, G.; Tamburini, A.; Del Conte, S.; Giannico, C. InSAR monitoring of tunnel induced ground movements. *Geomech. Tunneling* **2016**, *9*, 15–22, doi:10.1002/geot.201500052.

6. Samsonov, S. V.; Tiampo, K.F.; Feng, W. Fast subsidence in downtown of Seattle observed with satellite radar. *Remote Sens. Appl. Soc. Environ.* **2016**, *4*, 179–187, doi:10.1016/j.rsase.2016.10.001.

7. Massonnet, D.; Rossi, M.; Carmona, C.; Adragna, F.; Peltzer, G.; Feigl, K.; Rabaute, T. The displacement field of the Landers earthquake mapped by radar interferometry. *Nature* **1993**, *364*, 138–142, doi:10.1038/364138a0.

8. Zangerl, C.; Eberhardt, E.; Evans, K.F.; Loew, S. Consolidation settlements above deep tunnels in fractured crystalline rock: Part 2-Numerical analysis of the Gotthard highway tunnel case study. *Int. J. Rock Mech. Min. Sci.* **2008**, *45*, 1211–1225, doi:10.1016/j.ijrmms.2008.02.005.

9. Zangerl, C.; Evans, K.F.; Eberhardt, E.; Loew, S. Consolidation settlements above deep tunnels in fractured crystalline rock: Part 1-Investigations above the Gotthard highway tunnel. *Int. J. Rock Mech. Min. Sci.* **2008**, *45*, 1195–1210, doi:10.1016/j.ijrmms.2008.02.002.

10. Gabriel, A.K.; Goldstein, R.M.; Zebker, H.A. Mapping small elevation changes over large areas: differential radar interferometry. *J. Geophys. Res.* **1989**, *94*, 9183–9191, doi:10.1029/JB094iB07p09183.

11. Massonnet, D.; Feigl, K.L. Radar interferometry and its application to changes in the earth's surface. *Rev. Geophys.* **1998**, *36*, 441–500, doi:10.1029/97RG03139.

12. Ferretti, A.; Prati, C.; Rocca, F. Permanent scatterers in SAR interferometry. *IEEE Trans. Geosci. Remote Sens.* **2001**, *39*, 8–20, doi:10.1109/36.898661.

13. Hooper, A.; Zebker, H.; Segall, P.; Kampes, B. A new method for measuring deformation on volcanoes and other natural terrains using InSAR persistent scatterers. *Geophys. Res. Lett.* **2004**, *31*, 1–5, doi:10.1029/2004GL021737.

14. Berardino, P.; Fornaro, G.; Lanari, R.; Sansosti, E. A new algorithm for surface deformation monitoring based on small baseline differential SAR interferograms. *IEEE Trans. Geosci. Remote Sens.* **2002**, *40*, 2375–2383, doi:10.1109/TGRS.2002.803792.

15. Samsonov, S.; d'Oreye, N. Multidimensional time-series analysis of ground deformation from multiple InSAR data sets applied to Virunga Volcanic Province. *Geophys. J. Int.* **2012**, *191*, 1095–1108, doi:10.1111/j.1365-246X.2012.05669.x.

16. Pepe, A.; Solaro, G.; Calò, F.; Dema, C. A Minimum Acceleration Approach for the Retrieval of Multiplatform InSAR Deformation Time Series. *IEEE J. Sel. Top. Appl. Earth Obs. Remote Sens.* **2016**, *9*, 3883–3898, doi:10.1109/JSTARS.2016.2577878.

17. Yu, L.; Yang, T.; Zhao, Q.; Liu, M.; Pepe, A. The 2015-2016 ground displacements of the Shanghai coastal area inferred from a combined COSMO-SkyMed/Sentinel-1 DInSAR analysis. *Remote Sens.* **2017**, *9*, doi:10.3390/rs9111194.

18. Pepe, A.; Calò, F. A review of interferometric synthetic aperture RADAR (InSAR) multi-track approaches for the retrieval of Earth's Surface displacements. *Appl. Sci.* **2017**, *7*, doi:10.3390/app7121264.

19. Ebmeier, S.K.; Biggs, J.; Mather, T.A.; Amelung, F. Applicability of InSAR to tropical volcanoes: Insights from Central America. *Geol. Soc. Spec. Publ.* **2013**, *380*, 15–37, doi:10.1144/SP380.2.

20. Bekaert, D.P.S.; Hooper, A.; Wright, T.J. Journal of Geophysical Research : Solid Earth A spatially variable power law tropospheric correction technique for InSAR data. *J. Geophys. Res. Solid Earth* **2015**, 1–12, doi:10.1002/2014JB011557.A.

21. Lees, D.J.; Gunatilake, J. The Hydrogeology of the Central Highlands in Sri Lanka and its effect on tunnel construction. In Proceedings of the 16th Australasian Tunnelling Conference; 2017.

22. Nater, P.; Hazrati, M. Uma Oya Multi-Purpose Development Project: Lessons

Learned From Excavations Under High Stress Conditions. In Proceedings of the ISRM Progressive Rock Failure Conference; Ascona, Switzerland, 2017.

23. Wannenmacher, H.; Hosseini, A.; Wenner, D.; Rahbar, A.; Shahroki, Z. Water Ingress and Reduction Measures in the Headrace Tunnel at the Uma Oya Multipurpose Project. In Proceedings of the Hydro 2016; Montreux, 2016.

24. Rahbar, A.; Lees, D.J.; Hosseeini, A.H.; Shahrokhi, Z.; Wenner, D. The Design and Construction of Grouting against Water Ingress in the Headrace Tunnel for the Uma Oya Project , Sri Lanka. In Proceedings of the Proceedings of the World Tunnel Congress 2017 – Surface challenges – Underground solutions.; Bergen, Norway, 2017.

25. Ministry of Mahaweli Development and Environment *Annual Preformance Report Accounts 2017*; 2017;

26. Loew, S.; Lützenkirchen, V.; Hansmann, J.; Ryf, A.; Guntli, P. Transient surface deformations caused by the Gotthard Base Tunnel. *Int. J. Rock Mech. Min. Sci.* **2015**, *75*, 82–101, doi:10.1016/j.ijrmms.2014.12.009.

27. Kromer, R.A.; Abellán, A.; Hutchinson, D.J.; Lato, M.; Edwards, T.; Jaboyedoff, M. A 4D filtering and calibration technique for small-scale point cloud change detection with a terrestrial laser scanner. *Remote Sens.* **2015**, *7*, 13029–13058, doi:10.3390/rs71013029.

28. Zebker, H.A.; Amelung, F.; Jonsson, S. Remote sensing of volcano surface and internal processes using radar interferometry. *Geophys. Monogr. Ser.* **2000**, *116*, 179–205, doi:10.1029/GM116p0179.

29. Werner, C.; Wegmüller, U.; Strozzi, T.; Wiesmann, A. GAMMA SAR and interferometric processing software. *Eur. Sp. Agency, (Special Publ. ESA SP* **2000**, 211–219.

30. Hooper, A.J. A multi-temporal InSAR method incorporating both persistent scatterer and small baseline approaches. *Geophys. Res. Lett.* **2008**, *35*, 1–5, doi:10.1029/2008GL034654.

31. Hooper, A.; Zebker, H.A. Phase unwrapping in three dimensions with application to InSAR time series. *J. Opt. Soc. Am. A* **2007**, *24*, 2737, doi:10.1364/josaa.24.002737.

32. Hooper, A.; Bekaert, D.; Spaans, K.; Arikan, M. Recent advances in SAR interferometry time series analysis for measuring crustal deformation. *Tectonophysics* **2012**, *514–517*, 1–13, doi:10.1016/j.tecto.2011.10.013.

33. Bekaert, D.P.S.; Walters, R.J.; Wright, T.J.; Hooper, A.J.; Parker, D.J. Statistical

comparison of InSAR tropospheric correction techniques. *Remote Sens. Environ.* **2015**, *170*, 40–47, doi:10.1016/j.rse.2015.08.035.

34. Ebmeier, S.K.; Biggs, J.; Mather, T.A.; Amelung, F. On the lack of InSAR observations of magmatic deformation at Central American volcanoes. *J. Geophys. Res. Solid Earth* **2013**, *118*, 2571–2585, doi:10.1002/jgrb.50195.

35. Amelung, F.; Galloway, D.L.; Bell, J.W.; Zebker, H.A.; Laczniak, R.J. Sensing the ups and downs of Las Vegas: InSAR reveals structural control of land subsidence and aquifer-system deformation. *Geology* **1999**, *27*, 483–486, doi:10.1130/0091-7613(1999)027<0483:STUADO>2.3.CO;2.

36. Anderssohn, J.; Wetzel, H.U.; Walter, T.R.; Motagh, M.; Djamour, Y.; Kaufmann, H. Land subsidence pattern controlled by old alpine basement faults in the Kashmar Valley, northeast Iran: Results from InSAR and levelling. *Geophys. J. Int.* **2008**, *174*, 287–294, doi:10.1111/j.1365-246X.2008.03805.x.

37. Ismail, A. Uma Oya Development Project: Multi-purpose or multi-destructive? *Dly. Mirror* 2017.

38. Silva, M. Water leakage in Uma Oya Project decreased. *Adaderana* 2017.

39. Zangerl, C.; Eberhardt, E.; Loew, S. Ground settlements above tunnels in fractured crystalline rock: Numerical analysis of coupled hydromechanical mechanisms. *Hydrogeol. J.* **2003**, *11*, 162–173, doi:10.1007/s10040-002-0234-4.

40. Masset, O.; Loew, S. Hydraulic conductivity distribution in crystalline rocks, derived from inflows to tunnels and galleries in the Central Alps, Switzerland. *Hydrogeol. J.* **2010**, *18*, 863–891, doi:10.1007/s10040-009-0569-1.

41. Cooray, P. The Precambrian of Sri Lanka : a historical review. *Precambrian Res.* **1994**, *66*, 3–18.

42. Cooray, P. Structural Trends in the Central Highlands of Ceylon. *Bull. Ceylon Geogr. Soc.* **1954**, *8*, 49–56.

43. Terzaghi, K. Principles of soil mechanics, IV—Settlement and consolidation of clay. *Eng. News-Record* **1925**, *95*, 874–878.

44. Chambers, J.E.; Meldrum, P.I.; Wilkinson, P.B.; Ward, W.; Jackson, C.; Matthews, B.; Joel, P.; Kuras, O.; Bai, L.; Uhlemann, S.; et al. Spatial monitoring of groundwater drawdown and rebound associated with quarry dewatering using automated time-lapse electrical resistivity tomography and distribution guided clustering. *Eng. Geol.* **2015**, *193*, 412–420, doi:10.1016/j.enggeo.2015.05.015.

45. Chaussard, E.; Wdowinski, S.; Cabral-Cano, E.; Amelung, F. Land subsidence in

central Mexico detected by ALOS InSAR time-series. *Remote Sens. Environ.* **2014**, *140*, 94–106, doi:10.1016/j.rse.2013.08.038.

46. Chaussard, E.; Amelung, F.; Abidin, H.; Hong, S.H. Sinking cities in Indonesia: ALOS PALSAR detects rapid subsidence due to groundwater and gas extraction. *Remote Sens. Environ.* **2013**, *128*, 150–161, doi:10.1016/j.rse.2012.10.015.

47. Béjar-Pizarro, M.; Ezquerro, P.; Herrera, G.; Tomás, R.; Guardiola-Albert, C.; Ruiz Hernández, J.M.; Fernández Merodo, J.A.; Marchamalo, M.; Martínez, R. Mapping groundwater level and aquifer storage variations from InSAR measurements in the Madrid aquifer, Central Spain. *J. Hydrol.* **2017**, *547*, 678–689, doi:10.1016/j.jhydrol.2017.02.011.

48. Bonì, R.; Herrera, G.; Meisina, C.; Notti, D.; Béjar-Pizarro, M.; Zucca, F.; González, P.J.; Palano, M.; Tomás, R.; Fernández, J.; et al. Twenty-year advanced DInSAR analysis of severe land subsidence: The Alto Guadalentín Basin (Spain) case study. *Eng. Geol.* **2015**, *198*, 40–52, doi:10.1016/j.enggeo.2015.08.014.

49. Calderhead, A.I.; Therrien, R.; Rivera, A.; Martel, R.; Garfias, J. Simulating pumping-induced regional land subsidence with the use of InSAR and field data in the Toluca Valley, Mexico. *Adv. Water Resour.* **2011**, *34*, 83–97, doi:10.1016/j.advwatres.2010.09.017.

50. Coda, S.; Tessitore, S.; Di Martire, D.; Calcaterra, D.; De Vita, P.; Allocca, V. Coupled ground uplift and groundwater rebound in the metropolitan city of Naples (southern Italy). *J. Hydrol.* **2019**, *569*, 470–482, doi:10.1016/j.jhydrol.2018.11.074.

51. Motagh, M.; Shamshiri, R.; Haghshenas Haghighi, M.; Wetzel, H.U.; Akbari, B.; Nahavandchi, H.; Roessner, S.; Arabi, S. Quantifying groundwater exploitation induced subsidence in the Rafsanjan plain, southeastern Iran, using InSAR time-series and in situ measurements. *Eng. Geol.* **2017**, *218*, 134–151, doi:10.1016/j.enggeo.2017.01.011.

52. Wnuk, K.; Walton, G.; Zhou, W. Four-dimensional filtering of InSAR persistent scatterers elucidates subsidence induced by tunnel excavation in the Sri Lankan highlands. *J. Appl. Remote Sens.* **2019**, *13*, 1–16, doi:10.1117/1.jrs.13.034508.

53. Werner, C.; Lowry, B.; Wegmuller, U.; Pugh, N.; Schrock, G.; Zhou, W. Deformation time-series derived from terrestrial radar observations using persistent scatterer interferometry in Seattle, Washington. *Int. Geosci. Remote Sens. Symp.* **2016**, *November*, 6835–6838, doi:10.1109/IGARSS.2016.7730784.

54. Lowry, B.; Gomez, F.; Zhou, W.; Mooney, M.A.; Held, B.; Grasmick, J. High resolution displacement monitoring of a slow velocity landslide using ground based radar interferometry. *Eng. Geol.* **2013**, *166*, 160–169,

doi:10.1016/j.enggeo.2013.07.007.

55. Lowry, B.W.; Baker, S.; Zhou, W. A case study of novel landslide activity recognition using ALOS-1 InSAR within the ragged mountain Western Hillslope in Gunnison county, Colorado, USA. *Remote Sens.* **2020**, *12*, doi:10.3390/rs12121969.

56. Wang, G. ya; Zhu, J. qi; You, G.; Yu, J.; Gong, X. long; Li, W.; Gou, F. gang Land rebound after banning deep groundwater extraction in Changzhou, China. *Eng. Geol.* **2017**, *229*, 13–20, doi:10.1016/j.enggeo.2017.09.006.

57. Lu, Z.; Danskin, W.R. InSAR analysis of natural recharge to define structure of a ground-water basin, San Bernardino, California. *Geophys. Res. Lett.* **2001**, *28*, 2661–2664.

58. Troost, K.G.; Booth, D.B. Geology of Seattle and the Seattle area, Washington. *Geol. Soc. Am. Rev. Eng. Geol.* **2008**, *XX*, 1–35.

59. Jones, M.A. Geologic framework for the Puget Sound aquifer system, Washington and British Columbia. *US Geol. Surv. Prof. Pap.* **1999**.

60. Shannon & Wilson *Interim Settlement Evaluation Report Alaskan Way Viaduct Replacement Program*; 2015;

61. Vaccaro, J.J.; Hansen Jr., A.J.; Jones, M.A. Hydrogeologic framework of the Puget Sound aquifer system, Washington and British Columbia. *US Geol. Surv. Prof. Pap.* **1998**, *1424 D*, 77.

62. Hanke, R.; Rasband, L. *Bertha Rescue Shaft - SR99 Tunnel*. 2015, pp. 12–15.

63. Eppler, J.; Kubanski, M. Subsidence monitoring of the Seattle viaduct tunnelling project with Homogeneous Distributed Scatterer InSAR. In Proceedings of the Proceedings of the Ninth Symposium on Field Measurements in Geomechanics, Australian Centre for Geomechanics, Perth; 2015; pp. 303–314.

64. Brierley Associates *Ground Settlement from Dewatering During Construction*; 2015;

65. Clare, J. What comes down must go up-dewatering-induced ground movement on the SR-99 bored tunnel project, Seattle, WA, USA. In Proceedings of the North American Tunneling Conference, NAT 2018; 2018; Vol. 2, pp. 991–998.

66. Samsonov, S. V.; Tiampo, K.F. Monitoring of urban subsidence in coastal cities: Case studies Vancouver and Seattle. *2016 3rd Int. Conf. Digit. Inf. Process. Data Mining, Wirel. Commun. DIPDMWC 2016* **2016**, 36–39,

doi:10.1109/DIPDMWC.2016.7529360.

67. Ozawa, T.; Ueda, H. Advanced interferometric synthetic aperture radar (InSAR) time series analysis using interferograms of multiple-orbit tracks: A case study on Miyake-jima. *J. Geophys. Res. Solid Earth* **2011**, *116*, doi:10.1029/2011JB008489.

68. Cavur, M.; Moraga, J.; Sebnem Duzgun, H.; Soydan, H.; Jin, G. Displacement analysis of geothermal field based on psinsar and som clustering algorithms: A case study of Brady field, Nevada—USA. *Remote Sens.* **2021**, *13*, 1–22, doi:10.3390/rs13030349.

69. Chen, C.T.; Hu, J.C.; Lu, C.Y.; Lee, J.C.; Chan, Y.C. Thirty-year land elevation change from subsidence to uplift following the termination of groundwater pumping and its geological implications in the Metropolitan Taipei Basin, Northern Taiwan. *Eng. Geol.* **2007**, *95*, 30–47, doi:10.1016/j.enggeo.2007.09.001.

70. Waltham, T. Sinking cities. *Geol. Today* **2002**, *18*, 95–100, doi:10.1046/j.1365-2451.2002.00341.x.

71. Gambolati, G.; Teatini, P. Geomechanics of subsurface water withdrawal and injection. *Water Resour. Res.* **2015**, *51*, 3922–3955, doi:10.1002/2014WR016841.

72. Chilingarian, G. V.; Knight, L. Relationship Between Pressure and Moisture Content of Kaolinite, Illite, and Montmorillonite Clays. *Am. Assoc. Pet. Geol. Bull.* **1960**, *44*, 101–106, doi:10.1306/0bda5f81-16bd-11d7-8645000102c1865d.

73. Phien-wej, N.; Giao, P.H.; Nutalaya, P. Land subsidence in Bangkok, Thailand. *Eng. Geol.* **2006**, *82*, 187–201, doi:10.1016/j.enggeo.2005.10.004.

74. Peduto, D.; Nicodemo, G.; Maccabiani, J.; Ferlisi, S. Multi-scale analysis of settlement-induced building damage using damage surveys and DInSAR data: A case study in The Netherlands. *Eng. Geol.* **2017**, *218*, 117–133, doi:10.1016/j.enggeo.2016.12.018.

75. Tomás, R.; Márquez, Y.; Lopez-Sanchez, J.M.; Delgado, J.; Blanco, P.; Mallorquí, J.J.; Martínez, M.; Herrera, G.; Mulas, J. Mapping ground subsidence induced by aquifer overexploitation using advanced Differential SAR Interferometry: Vega Media of the Segura River (SE Spain) case study. *Remote Sens. Environ.* **2005**, *98*, 269–283, doi:10.1016/j.rse.2005.08.003.

76. Bru, G.; González, P.J.; Mateos, R.M.; Roldán, F.J.; Herrera, G.; Béjar-Pizarro, M.; Fernández, J. A-DInSAR monitoring of landslide and subsidence activity: A case of urban damage in Arcos de la Frontera, Spain. *Remote Sens.* **2017**, *9*, 1–17, doi:10.3390/rs9080787.

77. Burgmann, R.; Rosen, P.A.; Fielding, E.J. Synthetic aperture radar interferometry to measure earth's surface topography and its deformation. *Annu. Rev. Earth Planet. Sci.* **2000**, *28*, 169–209, doi:10.1146/annurev.earth.28.1.169.

78. Rosen, P.A.; Hensley, S.; Joughin, I.R.; Li, F.K.; Madsen, S.N.; Rodríguez, E.; Goldstein, R.M. Synthetic aperture radar interferometry. *Proc. IEEE* **2000**, *88*, 333–382, doi:10.1007/978-3-642-11741-1_11.

79. Short, N.; Brisco, B.; Couture, N.; Pollard, W.; Murnaghan, K.; Budkewitsch, P. A comparison of TerraSAR-X, RADARSAT-2 and ALOS-PALSAR interferometry for monitoring permafrost environments, case study from Herschel Island, Canada. *Remote Sens. Environ.* **2011**, *115*, 3491–3506, doi:10.1016/j.rse.2011.08.012.

80. Wempen, J.M.; McCarter, M.K. Comparison of L-band and X-band differential interferometric synthetic aperture radar for mine subsidence monitoring in central Utah. *Int. J. Min. Sci. Technol.* **2017**, *27*, 159–163, doi:10.1016/j.ijmst.2016.11.012.

81. Lu, Y.; Ke, C.Q.; Zhou, X.; Wang, M.; Lin, H.; Chen, D.; Jiang, H. Monitoring land deformation in Changzhou city (China) with multi-band InSAR data sets from 2006 to 2012. *Int. J. Remote Sens.* **2018**, *39*, 1151–1174, doi:10.1080/01431161.2017.1399474.

82. Solari, L.; Ciampalini, A.; Raspini, F.; Bianchini, S.; Zinno, I.; Bonano, M.; Manunta, M.; Moretti, S.; Casagli, N. Combined use of C- and X-band SAR data for subsidence monitoring in an urban area. *Geosci.* **2017**, *7*, doi:10.3390/geosciences7020021.

83. Du, Z.; Ge, L.; Li, X.; Hay-Man Ng, A. Subsidence monitoring over the Southern Coalfield, Australia using both L-Band and C-Band SAR time series analysis. *Remote Sens.* **2016**, *8*, 1–16, doi:10.3390/rs8070543.

84. Luo, X.; Wang, C.; Long, Y.; Yi, Z. Analysis of the decadal kinematic characteristics of the Daguangbao landslide using multi-platform time series InSAR observations after the Wenchuan earthquake. *J. Geophys. Res. Solid Earth* **2020**, 1–21, doi:10.1029/2019jb019325.

85. Qu, T.; Xu, Q.; Liu, C.; Li, Z.; Chen, B.; Dai, K. Radar remote sensing applications in landslide monitoring with multi-platform insar observations: A case study from China. *Int. Arch. Photogramm. Remote Sens. Spat. Inf. Sci. - ISPRS Arch.* **2019**, *42*, 1939–1943, doi:10.5194/isprs-archives-XLII-2-W13-1939-2019.

86. Liu, L.; Yu, J.; Chen, B.; Wang, Y. Urban subsidence monitoring by SBAS-InSAR technique with multi-platform SAR images: a case study of Beijing Plain, China. *Eur. J. Remote Sens.* **2020**, *53*, 141–153, doi:10.1080/22797254.2020.1728582.

87. Solano-Rojas, D.E.; Wdowinski, S.; Cabral-Cano, E.; Osmanoglu, B.; Havazli, E.; Pacheco-Martioónez, J. A multiscale approach for detection and mapping differential subsidence using multi-platform InSAR products. *Proc. Int. Assoc. Hydrol. Sci.* **2020**, *382*, 173–177, doi:10.5194/piahs-382-173-2020.

88. Wu, J.; Hu, F.; Tianliang, Y. Ground subsidece monitoring along the levee of Huangpu River by multi-platform high-resolution SAR images. *4th Int. Work. Earth Obs. Remote Sens. Appl. EORSA 2016 - Proc.* **2016**, 227–231, doi:10.1109/EORSA.2016.7552802.

89. Bekaert, D.P.S.; Jones, C.E.; An, K.; Huang, M.H. Exploiting UAVSAR for a comprehensive analysis of subsidence in the Sacramento Delta. *Remote Sens. Environ.* **2019**, *220*, 124–134, doi:10.1016/j.rse.2018.10.023.

90. Serrano-Juan, A.; Pujades, E.; Vázquez-Suñè, E.; Crosetto, M.; Cuevas-González, M. Leveling vs. InSAR in urban underground construction monitoring: Pros and cons. Case of la sagrera railway station (Barcelona, Spain). *Eng. Geol.* **2017**, *218*, 1–11, doi:10.1016/j.enggeo.2016.12.016.

91. Motagh, M.; Djamour, Y.; Walter, T.R.; Wetzel, H.U.; Zschau, J.; Arabi, S. Land subsidence in Mashhad Valley, northeast Iran: Results from InSAR, levelling and GPS. *Geophys. J. Int.* **2007**, *168*, 518–526, doi:10.1111/j.1365-246X.2006.03246.x.

92. Bürgmann, R.; Hilley, G.; Ferretti, A.; Novali, F. Resolving vertical tectonics in the San Francisco Bay Area from permanent scatterer InSAR and GPS analysis. *Geology* **2006**, *34*, 221–224, doi:10.1130/G22064.1.

93. Catalão, J.; Nico, G.; Hanssen, R.; Catita, C. Merging GPS and atmospherically corrected InSAR data to map 3-D terrain displacement velocity. *IEEE Trans. Geosci. Remote Sens.* **2011**, *49*, 2354–2360, doi:10.1109/TGRS.2010.2091963.

94. Henderson, S.T.; Pritchard, M.E. Time-dependent deformation of Uturuncu volcano, Bolivia, constrained by GPS and InSAR measurements and implications for source models. *Geosphere* **2017**, *13*, 1834–1854, doi:10.1130/GES01203.1.

95. Hu, J.; Ding, X.L.; Li, Z.W.; Zhang, L.; Zhu, J.J.; Sun, Q.; Gao, G.J. Vertical and horizontal displacements of Los Angeles from InSAR and GPS time series analysis: Resolving tectonic and anthropogenic motions. *J. Geodyn.* **2016**, *99*, 27–38, doi:10.1016/j.jog.2016.05.003.

96. Poland, M.P.; Bürgmann, R.; Dzurisin, D.; Lisowski, M.; Masterlark, T.; Owen, S.; Fink, J. Constraints on the mechanism of long-term, steady subsidence at

Medicine Lake volcano, northern California, from GPS, leveling, and InSAR. *J. Volcanol. Geotherm. Res.* **2006**, *150*, 55–78, doi:doi:10.1016/j.jvolgeores.2005.07.007.

97. Akbarimehr, M.; Motagh, M.; Haghshenas-Haghighi, M. Slope stability assessment of the sarcheshmeh landslide, northeast Iran, investigated using InSAR and GPS observations. *Remote Sens.* **2013**, *5*, 3681–3700, doi:10.3390/rs5083681.

98. Dzurisin, D.; Lisowski, M.; Wicks, C.W. Continuing inflation at Three Sisters volcanic center, central Oregon Cascade Range, USA, from GPS, leveling, and InSAR observations. *Bull. Volcanol.* **2009**, *71*, 1091–1110, doi:10.1007/s00445-009-0296-4.

99. Xue, X.; Freymueller, J.; Lu, Z. Modeling the Posteruptive Deformation at Okmok Based on the GPS and InSAR Time Series: Changes in the Shallow Magma Storage System. *J. Geophys. Res. Solid Earth* **2020**, *125*, 1–15, doi:10.1029/2019JB017801.

100. Papoutsis, I.; Papanikolaou, X.; Floyd, M.; Ji, K.H.; Kontoes, C.; Paradissis, D.; Zacharis, V. Mapping inflation at Santorini volcano, Greece, using GPS and InSAR. *Geophys. Res. Lett.* **2013**, *40*, 267–272, doi:10.1029/2012GL054137.

101. Gudmundsson, S.; Sigmundsson, F.; Carstensen, J.M. Three-dimensional surface motion maps estimated from combined interferometric synthetic aperture radar and GPS data. *J. Geophys. Res. Solid Earth* **2002**, *107*, ETG 13-1-ETG 13-14, doi:10.1029/2001jb000283.

102. Hu, X.; Lu, Z.; Pierson, T.C.; Kramer, R.; George, D.L. Combining InSAR and GPS to Determine Transient Movement and Thickness of a Seasonally Active Low-Gradient Translational Landslide. *Geophys. Res. Lett.* **2018**, *45*, 1453–1462, doi:10.1002/2017GL076623.

103. Chang, W.L.; Smith, R.B.; Farrell, J.; Puskas, C.M. An extraordinary episode of Yellowstone caldera uplift, 2004-2010, from GPS and InSAR observations. *Geophys. Res. Lett.* **2010**, *37*, 6–11, doi:10.1029/2010GL045451.

104. Johanson, I.A.; Bürgmann, R. Creep and quakes on the nothern transition zone of the San Andreas fault from GPS and InSAR data. *Geophys. Res. Lett.* **2005**, *32*, 1–5, doi:10.1029/2005GL023150.

105. Gourmelen, N.; Amelung, F.; Lanari, R. Interferometric synthetic aperture radar-GPS integration: Interseismic strain accumulation across the Hunter Mountain fault in the eastern California shear zone. *J. Geophys. Res. Solid Earth* **2010**, *115*, 1–16, doi:10.1029/2009JB007064.

106. Manzo, M.; Ricciardi, G.P.; Casu, F.; Ventura, G.; Zeni, G.; Borgström, S.; Berardino, P.; Del Gaudio, C.; Lanari, R. Surface deformation analysis in the Ischia Island (Italy) based on spaceborne radar interferometry. *J. Volcanol. Geotherm. Res.* **2006**, *151*, 399–416, doi:10.1016/j.jvolgeores.2005.09.010.

107. Pritchard, M.E.; Simons, M.; Rosen, P.A.; Hensley, S.; Webb, F.H. Co-seismic slip from the 1995 July 30 Mw = 8.1 Antofagasta, Chile, earthquake as constrained by InSAR and GPS observations. *Geophys. J. Int.* **2002**, *150*, 362–376, doi:10.1046/j.1365-246X.2002.01661.x.

108. Xiong, L.; Xu, C.; Liu, Y.; Wen, Y.; Fang, J. 3D displacement field of wenchuan earthquake based on iterative least squares for virtual observation and GPS/inSAR observations. *Remote Sens.* **2020**, *12*, doi:10.3390/rs12060977.

109. Delouis, B.; Giardini, D.; Lundgren, P.; Salichon, J. Joint inversion of InSAR, GPS, teleseismic, and strong-motion data for the spatial and temporal distribution of earthquake slip: Application to the 1999 İzmit mainshock. *Bull. Seismol. Soc. Am.* **2002**, *92*, 278–299, doi:10.1785/0120000806.

110. Yin, Y.; Zheng, W.; Liu, Y.; Zhang, J.; Li, X. Integration of GPS with InSAR to monitoring of the Jiaju landslide in Sichuan, China. *Landslides* **2010**, *7*, 359–365, doi:10.1007/s10346-010-0225-9.

111. Tong, X.; Sandwell, D.T.; Smith-Konter, B. High-resolution interseismic velocity data along the San Andreas Fault from GPS and InSAR. *J. Geophys. Res. Solid Earth* **2013**, *118*, 369–389, doi:10.1029/2012JB009442.

112. Wright, T.J.; Parsons, B.E.; Lu, Z. Toward mapping surface deformation in three dimensions using InSAR. *Geophys. Res. Lett.* **2004**, *31*, 1–5, doi:10.1029/2003GL018827.

113. Fialko, Y.; Sandwell, D.; Simons, M.; Rosen, P. Three-dimensional deformation caused by the Bam, Iran, earthquake and the origin of shallow slip deficit. *Nature* **2005**, *435*, 295–299, doi:10.1038/nature03425.

114. Fialko, Y.; Simons, M.; Agnew, D. The complete (3-D) surface displacement field in the epicentral area of the 1999 Mw7.1 Hector Mine earthquake, California, from space geodetic observations. *Geophys. Res. Lett.* **2001**, *28*, 3063–3066.

115. Hu, J.; Li, Z.W.; Ding, X.L.; Zhu, J.J.; Zhang, L.; Sun, Q. 3D coseismic Displacement of 2010 Darfield, New Zealand earthquake estimated from multi-aperture InSAR and D-InSAR measurements. *J. Geod.* **2012**, *86*, 1029–1041, doi:10.1007/s00190-012-0563-6.

116. Hu, J.; Ding, X.L.; Li, Z.W.; Zhu, J.J.; Sun, Q.; Zhang, L. Kalman-Filter-Based

Approach for Multisensor, Multitrack, and Multitemporal InSAR. *IEEE Trans. Geosci. Remote Sens.* **2013**, *51*, 4226–4239.

117. Hu, J.; Li, Z.W.; Ding, X.L.; Zhu, J.J.; Zhang, L.; Sun, Q. Resolving three-dimensional surface displacements from InSAR measurements: A review. *Earth-Science Rev.* **2014**, *133*, 1–17, doi:10.1016/j.earscirev.2014.02.005.

118. Dai, K.; Liu, G.; Li, Z.; Li, T.; Yu, B.; Wang, X.; Singleton, A. Extracting vertical displacement rates in Shanghai (China) with multi-platform SAR images. *Remote Sens.* **2015**, *7*, 9542–9562, doi:10.3390/rs70809542.

119. Gray, L. Using multiple RADARSAT InSAR pairs to estimate a full three-dimensional solution for glacial ice movement. *Geophys. Res. Lett.* **2011**, *38*, 1–6, doi:10.1029/2010GL046484.

120. Fuhrmann, T.; Garthwaite, M.C. Resolving three-dimensional surface motion with InSAR: Constraints from multi-geometry data fusion. *Remote Sens.* **2019**, *11*, doi:10.3390/rs11030241.

121. Zhu, W.; Zhang, X.; Liu, Z.; Zhu, Q. Spatiotemporal Characterization of Land Subsidence in Guandu (China) Revealed by Multisensor InSAR Observations. *J. Sensors* **2020**, *2020*, 1–13, doi:10.1155/2020/8855364.

122. Monserrat, O.; Crosetto, M.; Cuevas, M.; Crippa, B. The thermal expansion component of persistent scatterer interferometry observations. *IEEE Geosci. Remote Sens. Lett.* **2011**, *8*, 864–868, doi:10.1109/LGRS.2011.2119463.

123. Castellazzi, P.; Martel, R.; Galloway, D.L.; Longuevergne, L.; Rivera, A. Assessing Groundwater Depletion and Dynamics Using GRACE and InSAR: Potential and Limitations. *Groundwater* **2016**, *54*, 768–780, doi:10.1111/gwat.12453.

124. Donnellan, A.; Ludwig, L.G.; Parker, J.W.; Rundle, J.B.; Wang, J.; Pierce, M.; Blewitt, G.; Hensley, S. Earth and Space Science inferred from the 2014 La Habra earthquake. *Earth Sp. Sci.* **2015**, *2*, 1–8, doi:10.1002/2015EA000113.

125. Schaefer, L.N.; Lu, Z.; Oommen, T. Post-eruption deformation processes measured using ALOS-1 and UAVSAR InSAR at Pacaya Volcano, Guatemala. *Remote Sens.* **2016**, *8*, 1–15, doi:10.3390/rs8010073.

126. Schaefer, L.N.; Lu, Z.; Oommen, T. Dramatic volcanic instability revealed by InSAR. *Geology* **2015**, *43*, 743–746, doi:10.1130/G36678.1.

127. Wnuk, K.; Wauthier, C. Surface deformation induced by magmatic processes at Pacaya Volcano, Guatemala revealed by InSAR. *J. Volcanol. Geotherm. Res.* **2017**, *344*, 197–211, doi:10.1016/j.jvolgeores.2017.06.024.

128. Hu, X.; Bürgmann, R. Rheology of a Debris Slide From the Joint Analysis of UAVSAR and LiDAR Data. *Geophys. Res. Lett.* **2020**, *47*, 1–9, doi:10.1029/2020GL087452.

129. Delbridge, B.G.; Bürgmann, R.; Fielding, E.; Hensley, S.; Schulz, W.H. Three-dimensional surface deformation derived from airborne interferometric UAVSAR: Application to the Slumgullion Landslide. *J. Geophys. Res. Solid Earth* **2016**, *121*, 3951–3977, doi:10.1002/2015JB012559.

130. Hensley, S.; Wheeler, K.; Sadowy, G.; Jones, C.; Shaffer, S.; Zebker, H.; Miller, T.; Heavey, B.; Chuang, E.; Chao, R.; et al. The UAVSAR instrument: Description and first results. *2008 IEEE Radar Conf. RADAR 2008* **2008**, 0–5, doi:10.1109/RADAR.2008.4720722.

131. Rosen, P.A.; Hensley, S.; Wheeler, K.; Sadowy, G.; Miller, T.; Shaffer, S.; Muellerschoen, R.; Jones, C.; Zebker, H.; Madsen, S. Uavsar: A new NASA airborne SAR system for science and technology research. *IEEE Natl. Radar Conf. - Proc.* **2006**, 22–29, doi:10.1109/RADAR.2006.1631770.

132. Hensley, S.; Zebker, H.; Jones, C.; Michel, T.; Muellerschoen, R.; Chapman, B. First deformation results using the NASA/JPL UAVSAR instrument. *APSAR 2009 - 2009 Asia-Pacific Conf. Synth. Aperture Radar, Proc.* **2009**, 1051–1055, doi:10.1109/APSAR.2009.5374246.

133. Baker, G. *Regional Connector Transit Project Quarterly Project Status Report, March 2020*; 2020;

134. Zheng, H.; Mooney, M.; Gutierrez, M.; Bragard, C. *SEM deformation prediction and observation by 3D numerical analysis*; 2020;

135. Wegmüller, U.; Werner, C. Mitigation of thermal expansion phase in persistent scatterer interferometry in an urban environment. *2015 Jt. Urban Remote Sens. Event, JURSE 2015* **2015**, 3–6, doi:10.1109/JURSE.2015.7120505.

136. Tikhonov, A.N.; Arsenin, V.Y. *Solution of Ill-Posed Problems*; Wiley: New York, NY, USA, 1977;

137. Hansen, P.C.; O'leary, D.P. The Use of the L-Curve in the Regularization of Discrete Ill-Posed Problems. *SIAM J. Sci. Comput.* **1993**, *14*, 1487–1503.

138. Rezghi, M.; Hosseini, S.M. A new variant of L-curve for Tikhonov regularization. *J. Comput. Appl. Math.* **2009**, *231*, 914–924, doi:10.1016/j.cam.2009.05.016.

139. Hansen P.C. REGULARIZATION TOOLS: A Matlab package for analysis and solution of discrete ill-posed problems. *Numer. Algorithms* **1994**, *6*, 1–35.

140. Meldebekova, G.; Yu, C.; Li, Z. Quantifying Ground Subsidence Associated with Aquifer Overexploitation Using Space-Borne Radar Interferometry in Kabul, Afghanistan. *Remote Sens.* **2020**, *12*, doi:doi:10.3390/rs12152461.

141. Wanwan, Z.; Yinghai, K.; Huili, G.; Lin, Z.; Beibei, C. Monitoring of land surface deformation in Beijing with time-series InSAR technique based on multi-band InSAR data using RADARSAT-2 and TERRASAR-X. *4th Int. Work. Earth Obs. Remote Sens. Appl. EORSA 2016 - Proc.* **2016**, 260–264, doi:10.1109/EORSA.2016.7552809.

142. Sandwell, D.T.; Myer, D.; Mellors, R.; Shimada, M.; Brooks, B.; Foster, J. Accuracy and resolution of ALOS interferometry: Vector deformation maps of the father's day intrusion at Kilauea. *IEEE Trans. Geosci. Remote Sens.* **2008**, *46*, 3524–3534, doi:10.1109/TGRS.2008.2000634.

143. Hu, X.; Bürgmann, R.; Schulz, W.H.; Fielding, E.J. Four-dimensional surface motions of the Slumgullion landslide and quantification of hydrometeorological forcing. *Nat. Commun.* **2020**, *11*, 1–9, doi:10.1038/s41467-020-16617-7.

APPENDIX A – TECHNOLOGY TRANSFER ACTIVITIES

1 Accomplishments

1.1 What was done? What was learned?

- Development of a novel 4-D filtering algorithm, designed to remove phase noise from InSAR data acquired in highly vegetated, tropical locations, to a widespread subsidence event in the highlands of Sri Lanka

- Adaptation and testing of previously published algorithms that resolve satellite InSAR measurements into vertical and horizontal motion through a case study of subsidence events in Seattle, Washington, USA to reveal heterogeneous rebound and additionally delayed subsidence

- Development of novel modification to the minimum-acceleration algorithm, allowing it to combine multiplatform SAR data, especially to ingest airborne InSAR data, and produce true 3D (Vertical, East-West, and North-South) deformation time series of a small magnitude, spatially acute tunneling-induced subsidence event in Los Angeles, California, USA.

1.2 How have the results been disseminated?

- Results have been disseminated via poster sessions, conference presentations, and publication in peer-reviewed scientific journals

2 Participants and Collaborating Organizations

Name: Colorado School of Mines
Location: Golden, Colorado, USA
Contribution: Software and research space on campus

3 Outputs

Journal publications

Wnuk, K., Zhou, W., and Gutierrez, M., 2021, Mapping urban excavation induced deformation in 3D via multiplatform InSAR time-series: Remote Sensing, *accepted*.

Wnuk, K., Zhou, W., and Gutierrez, M., 2021, Tunneling-induced rapid differential ground rebound and delayed subsidence in an urban environment: *in prep*.

Wnuk, K., Walton, G., and Zhou, W., 2019, Four-dimensional filtering of InSAR persistent scatterers elucidates subsidence induced by tunnel excavation in the Sri Lankan highlands: Journal of Applied Remote Sensing, v. 13, no. 03, p. 1–16, doi: 10.1117/1.jrs.13.034508.

Presentations

Wnuk, K., Zhou, W., Gutierrez, M. “Rapid Urban Rebound Measured by Satellite InSAR.” Department of Geology and Geological Engineering Research Fair, Golden, CO. March 2020.

Wnuk, K., Zhou, W., Walton, G. “InSAR Analysis of Surface Subsidence above a Headrace Tunnel in the Sri Lankan Highlands.” Association of Environmental and Engineering Geologists Annual Meeting, San Francisco, CA. September 2018.

Wnuk, K., Zhou, W., Walton, G. “InSAR Analysis of Surface Subsidence above a Headrace Tunnel in the Sri Lankan Highlands.” Graduate Research and Discovery Symposium, Golden, CO. April 2018.

Wnuk, K., Zhou, W., Gutierrez, M. “Using InSAR Time Series Analysis to Characterize Tunnel Induced Surface Deformation.” Association of Environmental and Engineering Geologists Annual Meeting, Colorado Springs, CO. September 2017.

4 Outcomes

Post-processing through either 4-D filtering or application of the MinA algorithm revealed the true extent of surface displacements that were previously unrecognized or not captured by ground-based data. Knowing the full extent, duration, and magnitude of excavation-induced subsidence can be crucial to mitigating their potential impacts. This research highlights the need for space based geodetic monitoring of tunneling projects, and offers practical solutions for its application. As more SAR platforms become available, including the recent launch of the SAOCOM SAR constellation and future launch of NASA-ISRO SAR mission, post-processing algorithms can be used to combine data from multiple SAR inputs to compare to or potentially replace ground based geodetic systems for monitoring purposes.

5 Impacts

Standard InSAR analyses can only make measurements within a single viewing geometry and can be impacted by noise when applied to vegetated areas or tropical areas subject to turbulent atmospheric changes. High-resolution InSAR data from a new generation of satellites combined with state of the art post-processing algorithms can enhance InSAR time-series data and reduce noise. The research projects described in this report are designed to reduce remaining data noise and resolve tunneling-induced subsidence in three dimensions using space and airborne based observation. The report illustrates the impacts of post-processing of large, temporally dense LOS InSAR time-series datasets can have on reduction of interferometric noise and more accurate and precise maps and measurements of subsidence in both natural and urban environments.

APPENDIX B - DATA FROM THE PROJECT

All data used for InSAR analyses, aside from commercially available COSMO-SkyMed, are available for free from NASA JPL (https://uavsar.jpl.nasa.gov/cgi-bin/data.pl) or the Alaska Satellite Facility (https://search.asf.alaska.edu/). The time range, number of acquisitions, acquisition modes, and track and frame values are available in Chapters 2, 3, and 4. Digital Elevation Models used are available at earth explorer (https://earthexplorer.usgs.gov/) and the national map (https://apps.nationalmap.gov/downloader/#/).